**Modelling spinal locomotor circuits for movements in developing zebrafish**

Roussel, Yann[1,2], Gaudreau, Stephanie F.[1], Sengupta, Mohini[3], and Bui, Tuan V.[1]

[1]Brain and Mind Research Institute, Centre for Neural Dynamics, Department of Biology, University of Ottawa, Ottawa, Canada, K1N 6N5
[2]Blue Brain Project, École Polytechnique Fédérale de Lausanne, Genève, Switzerland, CH-1202
[3]Washington University School of Medicine, Department of Neuroscience, St Louis, MO, USA

**Corresponding author:**
Tuan Vu Bui
Tuan.bui@uottawa.ca

Conflict of interest: The authors declare no competing financial interests.

**Acknowledgments**: We would like to thank Martha Bagnall, Vamsi Daliparthi, Joe Fetcho, Sara Goltash, Michael Hildebrand, Emily Kacer, Alex Laliberte, Nicolas Lalonde, John Lewis, Aaron Shifman, and Emily Standen for advice related to the modelling and critical discussion of this manuscript. This research was supported by an NSERC Discovery Grant (RGPIN-2015–06403) and a McDonnell Center for Cellular and Molecular Neurobiology Postdoc Fellowship FY21.

## ABSTRACT

Many of the neural components of spinal circuits dedicated to locomotor control have been identified in the developing zebrafish. How these circuits operate together to generate the various swimming movements during development remains to be clarified. In this study, we iteratively construct models of zebrafish spinal circuits coupled to simplified musculoskeletal models that reproduce several developmental locomotor movements of zebrafish. The models replicate published experimental results examining the roles of synaptic excitation and inhibition and specific spinal populations to locomotor movements. Also, the models identify other possible mechanisms underlying the generation of locomotor movements by developing zebrafish. Notably, our modelling work demonstrates how the site of rhythm generation could transition between coiling and swimming, underlines the importance of contralateral excitation to multiple tail beats, and estimates the sensitivity of spinal locomotor networks to motor command amplitude, synaptic weights and firing behaviour.

## INTRODUCTION

Movements made in the early stages of development can be critical for the survival of many species. The escape response seen in various fish and amphibians is one such example of a vital movement present at early developmental stages (Domenici & Hale, 2019). However, the nervous system's control of movement does not come fully formed but matures as the nervous system develops (Favero et al., 2014). This maturation enables a broader repertoire of movements to arise. During this process, new neurons are born and subsequently integrated into neural circuits that are newly formed or refined, presumably leading to the emergence of more and more coordinated and skillful movements. Determining how the formation of new neurons and circuits leads to the emergence of different movements can provide valuable insights into the role of distinct neurons or circuits in motor control.

The maturation of swimming in developing zebrafish has been well described at both the ethological and the cellular level (Drapeau et al., 2002; McLean & Fetcho, 2009). Single strong body bends on one side of the body, also known as coils, emerge during the first day of development at around 17 hours post-fertilization (hpf) as the earliest locomotor behaviour (Saint-Amant & Drapeau, 1998). Single coils are quickly followed by double coils (i.e. two successive coils, one for each side of the body) at around 24 hpf (Knogler et al., 2014). Touch-evoked swimming appears around 27 hpf as coiling begins to subside. Spontaneous swimming movements emerge around 3 dpf (Saint-Amant, 2010). One form of swimming is beat-and-glide swimming, which is characterized as trains of multiple shorter episodes (hundreds of milliseconds long) interspaced by quiescent (or "gliding") periods (Drapeau et al., 2002).

During this rapid series of transitions between locomotor maneuvers, populations of spinal neurons are progressively generated, starting with primary motoneurons at about 9 hpf. Subsequently, spinal motoneurons and interneurons are generated in stereotyped spatiotemporal birth orders (Kimmel et al., 1994; Myers et al., 1986; Satou et al., 2012). Two successive waves of axogenesis occur in the embryonic spinal cord (Bernhardt et al., 1990). The first wave occurs around 16-17 hpf. It includes axon growth in primary motoneurons (MNs) that innervate both red and white muscle fibres at early developmental stages (Buss & Drapeau, 2000). Primary MNs enable coiling and escape movements (Kimmel et al., 1995; Saint-Amant & Drapeau, 2000). Several spinal interneurons that are also important for early movements extend their axons along with primary MNs. These include Ipsilateral Caudal (IC) interneurons thought to play an essential role in driving the rhythm of early locomotor behaviour due to their endogenous bursting activity (Tong & McDearmid, 2012). The second wave of axon growth occurs at around 23-25 hpf. It involves axon growth in secondary motoneurons involved with slower movements (Liu & Westerfield, 1988) and spinal interneuron populations that include excitatory and inhibitory, ipsilaterally and contralaterally as well as ascending and descending projecting subtypes (Bernhardt et al., 1990;

Higashijima et al., 2004). The progressive generation of different populations of spinal neurons and their axonal outgrowth during a time when the zebrafish is expanding its locomotor repertoire suggests that the incorporation of new circuits consisting of new populations of spinal neurons into existing locomotor circuits underlies the transition between different locomotor maneuvers.

We have recently provided evidence that the maturation from coiling to later stages of swimming is accompanied by an operational switch in how spinal locomotor circuits generate the rhythm underlying tail beats. Specifically, we demonstrated spinal circuits transitioned from relying upon pacemakers with endogenous bursting properties during coiling towards depending upon network oscillators whose rhythm is driven by excitatory and inhibitory synapses (Roussel et al., 2020).

In light of these and earlier findings describing the composition and maturation of spinal locomotor circuits, we sought to generate computational models that replicate developmental locomotor movements of the zebrafish. We iteratively constructed models for several locomotor movements by incorporating specific spinal populations, shifts in relative connection strength and changes in the firing behaviour of neurons. While computational modelling has generated invaluable insights into the function and mechanisms of spinal locomotor circuits of several species (Ausborn et al., 2019; Bicanski et al., 2013; Danner et al., 2019; Hull et al., 2016; Kozlov et al., 2014; Sautois et al., 2007), there is to our knowledge no such model for the developing zebrafish spinal cord. Here, we build one of the first developmental models of the zebrafish spinal locomotor circuit that can accurately reproduce predominant locomotor behaviours during early zebrafish development. In the process, we test theories about the possible contributions of specific neural circuits and spinal populations to locomotor movements in zebrafish and identify untested hypotheses on the operation of spinal locomotor networks in developing zebrafish.

## RESULTS

We aimed to model how spinal locomotor circuits may develop through the integration of spinal interneurons and the modification of synaptic weights and firing behaviour over the first few days of development to enable the emergence of new locomotor movements. Our approach was to build an initial model based upon previously reported experimental observations of spinal circuits when the first locomotor movements emerge in zebrafish around 1 day post-fertilization (dpf). We then successively built upon this initial model to replicate several locomotor movements of the developing zebrafish.

The models were composed of single compartment neurons whose firing dynamics were determined by a small set of differential equations (Izhikevich, 2007). The firing of motoneurons was converted to muscle output. This output was used to estimate body angle and locomotor activity during simulations (Fig. 1). The composition of each model depended on the developmental stage and the locomotor movement to be generated.

### *Single coiling results from unilateral gap-junction coupling*

Coiling, which is already observed at 1 dpf, is characterized by a single strong, slow (hundreds of ms in duration) tail beat on one side of the body followed by a return to resting position (Saint-Amant & Drapeau, 1998). Coiling events are relatively infrequent, reaching a maximum frequency of 1 Hz around 20 hpf (Saint-Amant & Drapeau, 1998). Previous studies have established that this behaviour is generated by a spinal circuit relying mostly on gap junctions (i.e. electrical synapses) (Saint-Amant & Drapeau, 2001). The application of a gap junction blocker, heptanol, but not glutamatergic and glycinergic antagonists, suppressed spinal activity responsible for coiling. It has been proposed that rostrally-located IC pacemaker spinal neurons expressing persistent sodium currents ($I_{Na,P}$; (Tong & McDearmid, 2012)) drive periodic depolarizations of ipsilateral MNs via electrical synapses (Drapeau et al., 2002; Saint-Amant & Drapeau, 2001). Blocking glycinergic transmission does not prevent coiling or rhythmic activity. However, glycinergic synaptic bursts are observed in MNs during contralateral coiling events (Saint-Amant & Drapeau, 2001). These synaptic bursts have been proposed to arise from contralaterally projecting glycinergic neurons (Saint-Amant & Drapeau, 2000).

NETWORK DESCRIPTION Based upon the experimental observations reported above, we modelled the following architecture for the spinal locomotor circuit underlying coiling (Fig. 2*A*). Rostrocaudal chains of electrically coupled neurons were driven by a kernel of recurrently connected pacemakers (PMs, five for each kernel). One chain consisted of ten MNs (recall that each muscle in our model represents three somites in the coiling models). The other chain consisted of ten contralaterally projecting commissural inhibitory neurons that we named CINs. PMs were modeled on IC neurons. IC neurons have been reported to project caudally through multiple somites (Bernhardt et al., 1990). Electrical coupling between many populations of early-born

spinal neurons has been previously demonstrated, including between IC and motoneurons (Saint-Amant & Drapeau, 1998). Therefore, in addition to their recurrent connections, each PM formed electrical synapses with several rostral MNs and CINs (the first five of each ipsilateral chain in our model). Coupling between IC neurons and commissural inhibitory neurons has not been demonstrated yet. We based our electrical coupling between PMs and CINs on the fact that glutamatergic blockers do not block glycinergic synaptic bursts present at this stage (Saint-Amant & Drapeau, 2001), suggesting that gap-junctions mediate the activation of CINs underlying these bursts.

The connectivity within the chains was identical for both MNs and CINs chains. Each neuron in a chain formed electrical synapses with its three nearest rostral neighbours and its three nearest caudal neighbours within the same chain. There was also electrical coupling across the two ipsilateral chains as MNs formed gap junctions with the three nearest rostral and three nearest caudal CINs and vice-versa. Paired-recordings of MNs and CINs at this stage have yet to be published. Our assumption that MNs and CINs are electrically coupled at this stage was based upon the widespread electrical coupling between ipsilateral spinal neurons (Saint-Amant & Drapeau, 2001). To reproduce the glycinergic bursts observed in MNs at this stage (Saint-Amant & Drapeau, 2001), CINs projected to contralateral MNs. Thus, CINs formed glycinergic synapses with contralateral MNs and PMs. All CINs sent ascending projections to contralateral PMs. CINs projected to contralateral MNs within five to six segments so that the $i^{th}$ CIN projected to all contralateral MNs between the $i-5$ and $i+5$ segments.

Parameter values of PMs were chosen such that they exhibited a relatively depolarized threshold of action potentials and short action potentials as seen in experimental recordings in embryonic zebrafish (Tong & McDearmid, 2012). They were also modelled to exhibit periodic bursts lasting hundreds of ms in response to a constant tonic drive (Fig. 2*B*). This was accomplished in part by having a low value of $a$, the rate of the recovery variable $u$, and a relatively depolarized value of $c$, the reset potential after a spike is fired. MNs and CINs were modelled to generate tonic firing (Fig. 2*B*). Finally, to activate the circuit, a constant drive was provided to the left PMs only. Restricting the drive to left PMs prevented the appearance of multiple coils due to near-coincident bilateral coils.

SIMULATION RESULTS Our simulations show that this model can generate single coils characterized by large body bends to one side of the body lasting approximately one second (Fig. 2*C*, *Supp. Data video S1*). Our base single coiling model generated six evenly interspersed single coils during a 10 s simulation. This 0.6 Hz coiling frequency is within the range of frequencies observed during zebrafish development (Saint-Amant & Drapeau, 1998).

Previously reported whole-cell patch-clamp recordings of MNs at this developmental stage display two typical events (Saint-Amant & Drapeau, 2001): periodic depolarizations (PDs) via electrical

synapses and synaptic bursts (SBs) from contralateral spinal glycinergic neurons. These events last hundreds of ms. In our model, SBs were observed in the contralateral PMs and MNs (events during coilings in left neurons seen in the grey traces in Figure 2*C*). SBs were caused by glycinergic input from CINs activated during the ipsilateral coilings. PDs can be observed in hyperpolarized motoneurons during ipsilateral coils (Fig. 2*D*).

The base model's sensitivity to variability was tested by running sets of five 20-s long simulations at various values of $\sigma_d$, $\sigma_p$and $\sigma_w$. The single coiling model's suitability was assessed by the relative absence of truncated coils, which were movements with only partial contractions restricted to the body's rostral segments (*Supp. Data video S2*). When $\sigma_d$ was incremented by 0.5 up to 4.5 while keeping $\sigma_p$ and $\sigma_w$ fixed at 0, the model generated 12.2 ± 1.5 coils per run (mean ± S.D.; *n* = 85 runs). Truncated coils were observed at $\sigma_d$= 3.5 (one out of five runs) and 4.5 (three out of five runs). Within these four runs, 2.2 ± 1.9 truncated coils were observed (12.7 ± 1.0 total coils per run, *n* = 4 runs). When $\sigma_p$ was incremented by 0.01 between 0.01-0.09 while keeping $\sigma_d$ and $\sigma_w$ fixed at 0, the model generated 12.1 ± 2.2 coils per run (*n* = 45 runs). Between $\sigma_p$= 0.06-0.09, seven out of twenty simulations had coils that were partially truncated (11.7 ± 4.2 truncated coils per run, 13.7 ± 1.4 total coils per run, *n* = 7 runs). Finally, when $\sigma_w$ was incremented by 0.1 between 0.1-1.0, the model generated 12.0 ± 0.3 coils per run (*n* = 50 runs; approximately 0.6 Hz). However, between $\sigma_w$= 0.5-1.0, nine out of thirty simulations had single coils that were partially truncated (10.2 ± 2.6 truncated coils per run; 12.3 ± 0.5 total coils per run, *n* = 7 runs). In sum, the single coiling model's sensitivity testing suggests that the model is more robust to variability in the synaptic weights and the tonic motor command drive and more sensitive to variability in the parameters that set the membrane potential dynamics of neurons.

Overall, the model captured this first locomotor behaviour of zebrafish in terms of the duration and frequency of coiling events as well as synaptic events of motoneurons. We then built upon this model to try to replicate the next step in the development of locomotion: the appearance of double coiling.

### *Double coiling is generated by a balance between excitatory and inhibitory commissural neurons*

After single coils appear, double coils emerge as a transitory locomotor behaviour during the same first day of development, coexisting with the single coiling behaviour. Double coiling is characterized by two successive coils, one on each side of the body, and lasts about one second (Knogler et al. 2014). Knogler et al. (2014) demonstrate that, at its peak frequency, double coiling can represent nearly three-quarters of all coiling events, with the rest being mostly single coils.

At the stage at which double coiling appears, the previous electrical scaffold for single coils seems to be supplemented with chemical glutamatergic synapses to form a hybrid electrical-chemical circuit. Adding CNQX and APV to block glutamatergic transmission precluded double coils while

sparing single coils (Knogler et al., 2014). In contrast, blocking glycinergic synapses led to triple or even quadruple coils (Knogler et al., 2014). As concluded by Knogler et al. (2014), these experimental observations suggest that some form of synaptic excitation is required for successive coils after a first coil. Glycinergic transmission seems to prevent the generation of more than two successive coils. Patch-clamp recordings of MNs at this developmental stage exhibit the same isolated PDs and SBs from earlier developmental stages and show mixed events in which a PD event directly follows an SB or vice-versa (Knogler et al., 2014). Interestingly, the application of CNQX eliminates mixed PD-SB events but not single isolated SBs, suggesting that the coupling of PD and SB in mixed events is glutamatergic (Knogler et al., 2014). Therefore, we aimed to generate a model with the following characteristics: 1) double coils lasting about one second in duration accounting for over half of the coiling events, 2) a dependence of double coiling upon excitatory synaptic transmission, 3) an increase in multiple coiling events in the absence of inhibitory synaptic transmission, and 4) the presence of mixed PD-SB events with similar sensitivity to the blockade of excitatory synaptic transmission as double coils.

NETWORK DESCRIPTION To implement a model capable of generating double coils that depend upon glutamatergic transmission, we built upon the single coiling model by adding two populations of neurons. To trigger a second contralateral coil, we added a population of commissural excitatory neurons (CENs, ten neurons for each side) electrically coupled to the previous scaffold (i.e. the ipsilateral PM-MN-CIN scaffold). CENs were arranged in a rostrally located chain within the spinal cord (Fig. 3*A*). Electrical synapses were formed with neighbouring MNs, CINs and CENs (the nearest three of each type of neuron in both the rostral and the caudal direction). Some ipsilateral PMs were coupled with the most rostral CENs.

The second population of neurons that we added were ipsilaterally projecting excitatory neurons present at this stage and shown to receive mixed PD-SB events (Knogler et al., 2014). These neurons have been suggested to be circumferential ipsilateral descending neurons (CiDs). We incorporated these neurons in the model (referred to as Ipsilateral Excitatory Descending or IEDs), where they were electrically coupled to PM neurons and projected glutamatergic synapses to CENs. CiDs most likely excite motoneurons as well, based upon the data from Knogler et al. (2014). Still, we omitted this connection as it was not necessary for double coilings to be generated. As CiDs display SBs at this stage, we modelled glycinergic projections from CINs to contralateral IEDs within five to six segments. The $i^{th}$ CIN projected to all contralateral IEDs between the $i$-$5$ and $i+5$ segments in a manner similar to how CINs project to contralateral MNs.

Both PMs received a tonic command though we delayed the activation of the tonic command to the right side by 1,500 ms to ensure that double coils were not near-coincident bilateral single coils. We modified several parameters of the PMs, most notably increases in the *a* parameter and the *k* parameter to enable a more extended inter-coiling period as reported by (Knogler et al., 2014).

The *a* parameter represents the time scale of the recovery variable *u* that returns the membrane potential to rest. The *k* parameter shapes subthreshold dynamics.

To generate the crossing excitation underlying the second coils, all CENs projected glutamatergic synapses with contralateral PMs. PMs continued to receive glycinergic inputs from contralateral CINs, putatively to prevent the generation of more than two successive coiling events (Knogler et al. 2014).

SIMULATIONS RESULTS Simulations of the double coiling model frequently generated pairs of successive, left-right alternating coils lasting about one second in total (Fig. 3*B*, *Supp. Data video S3*). In five 100-s long runs of the base model with a small amount of variability added to model parameters, 60% of events were double coils, with the rest mostly being single coils (31%), and very few triple coils or truncated single coils (5% each) (Fig. 3*H*).

The timing of activity of PMs, IEDs and CENs (Fig. 3*C*) suggests that double coils were generated by ipsilateral recruitment of IEDs and CENs during the first coil, which then led to activation of the contralateral PMs to initiate the second coil. A key to generating double coils in our model was to delay the activation of CENs. This delay enabled the activation of contralateral PMs after the first coiling is completed and when commissural inhibition of the contralateral PM has also terminated. If the activation of ipsilateral CENs occurred too early during the first coiling, which can be produced by increasing the weight of the IED to CEN and the CEN to contralateral PM glutamatergic synapses, the occurrence of a second coil is less likely (Fig. 3*D,H, Supp. Data video S4*).

To further underscore the importance of glutamatergic transmission to double coiling as reported experimentally (Knogler et al., 2014), blocking glutamatergic transmission in the model greatly reduced the number of double coils (Fig. 3*E,H, Supp. Data video S5*). On the other hand, blocking glycinergic synapses lead to an increase of multiple coilings of 3 or more coils (Fig. 3*F,H, Supp. Data video S6*) as reported by Knogler et al. (2014). This effect presumably occurs due to the unopposed reverberating commissural excitation of PMs by CENs.

In motoneurons hyperpolarized to prevent spiking, membrane potential traces exhibited mixed SB-PD or PD-SB events (Fig. 3*G*) observed experimentally (Knogler et al. 2014). The PDs were generated by gap-junction coupled PMs, whereas contralateral CINs generated the SBs.

The base model's sensitivity to variability was tested by running sets of five 100-s long simulations at various values of $\sigma_d, \sigma_p$and $\sigma_w$. The suitability of the double coiling model was assessed by the relative absence of multiple coils (more than two successive coils), abnormally sequenced (e.g. two rapid successive ipsilateral coils) and truncated coils. A model with a particular variability level was deemed unsuitable if it averaged more than one multiple coils or truncated coils during

the five runs. During testing for sensitivity to the motor command drive, $\sigma_d$ was incremented by 0.5 up to 3.0 while keeping $\sigma_p$ and $\sigma_w$ fixed at 0. The model became unsuitable at $\sigma_d$ = 2.5 (1.6 ± 1.3 unsuitable event per run, n = 11.6 ± 1.1 events per run, N = 5 runs). The model was unsuitable at $\sigma_d$ = 3.0 (2.6 ± 1.8 unsuitable events per run, n = 13.0 ± 2.3 events per run, N = 5 runs) as well. During testing for sensitivity to the parameters controlling the membrane potential dynamics, $\sigma_p$ was incremented by 0.01 up to 0.04 while keeping $\sigma_d$ and $\sigma_w$ fixed at 0. At $\sigma_p$= 0.03, one run out of five showed no activity, while one run showed four truncated coils and an abnormally sequenced coiling event. The three remaining runs exhibited double and single coils. At $\sigma_p$ = 0.04, all runs were unsuitable (9.0 ± 3.3 unsuitable events per run, n = 13.6 ± 3.6 events per run, N = 5 runs). Finally, during testing for sensitivity to the synaptic weights, $\sigma_w$ was incremented by 0.1 up to 0.5 while keeping $\sigma_d$ and $\sigma_p$ fixed at 0. The model became unsuitable at $\sigma_w$ = 0.3 (3.0 ± 1.5 unsuitable event per run, n = 10.4 ± 1.7 events per run, N = 5 runs) and $\sigma_w$ = 0.5 (2.6 ± 3.8 unsuitable event per run, n = 11.8 ± 4.7 events per run, N = 5 runs; no double coils were observed in three out of five runs). Like the single coiling model, the double coiling model seemed to be most sensitive to variability in the parameters that shape membrane potential dynamics and least sensitive to the motor command drive's amplitude.

### *Generation of swimming pattern by spinal network oscillators*

Around 2 or 3 dpf, zebrafish transition from coiling movements to swimming (Drapeau et al., 2002; Saint-Amant & Drapeau, 1998). This transition entails two fundamental changes in locomotor movements: First, locomotor movements consisting of long, slow coils are replaced by quick, short tail beats; and secondly, the number of consecutive tail beats are increased from the two side-to-side coilings seen in double coils to multiple consecutive tail beats that compose each swimming episode. The first swimming movement zebrafish exhibit is burst swimming characterized by long (1 s long) but infrequent episodes of tail beats. Burst swimming is then replaced by beat-and-glide swimming characterized by shorter (several hundreds of ms long) but more frequent episodes. Swim episodes in both swimming forms consist of repetitive left-right alternating, low-amplitude tail beats that propagate from the rostral toward the caudal end of the fish body and are generated at 20 to 80 Hz.

Beat-and-glide swimming can be produced in isolated larval zebrafish spinal cord preparations by NMDA application (Lambert et al., 2012; McDearmid & Drapeau, 2006; Wiggin et al., 2012) or by optogenetic stimulation of excitatory spinal neurons (Wahlstrom-Helgren et al., 2019). This capacity suggests that the transition from coiling to swimming episodes involves a delegation of rhythm generation from PMs to spinal locomotor circuits. Therefore, we sought to model a spinal network that could generate beat-and-glide swimming activity hallmarks - swim episodes lasting about 200-300 ms with repeated left-right alternating low-amplitude tail beats at around 20-40 Hz (slow swimming).

Recent experimental studies have also started to delineate the contributions of specific populations of spinal neurons to swimming. Ablation of ipsilaterally projecting, excitatory neurons in the V2a population eliminates swimming activity (Eklof-Ljunggren et al., 2012). Genetic ablation of ipsilaterally projecting, inhibitory neurons in the V1 population affects swim vigour but has no effects on the patterning of swimming (Kimura & Higashijima, 2019). Genetic ablation of a subset of commissural inhibitory neurons in the dI6 population reduces left-right alternation (Satou et al., 2020). We sought to replicate the role of these neurons in our model.

NETWORK DESCRIPTION We modified the previous model for double coiling to accommodate swimming (Fig. 4*A*). Whereas the PM populations' activity greatly influenced the frequency of coils and the side at which coils were made, we sought to place the control of tail beat rhythm and the alternation between left and right during swimming to the level of circuits in the spinal cord.

First, to emulate the body growth that occurs when zebrafish transition between coiling behaviours and swimming (Kimmel et al. 1995), we increased the size of the fish from ten to fifteen segments. Thus, each model somite in our swimming model represented two biological somites as opposed to three in our coiling model. PM neurons (homologs of IC neurons) were removed from the model to reduce computational load. We are not aware of any experimental evidence of the involvement of PM neurons in later swimming stages. Chains of MNs and CINs were increased from ten to fifteen neurons per side, while CENs were increased from ten to eleven neurons per side, and IEDs were increased from ten to twelve per side. Preliminary versions of the model suggested that longer chains of IEDs and CENs were likely to trigger the caudal segments too early, disturbing the overall swimming pattern. We thus decreased the length of IEDs and CENs chains until the desired pattern was restored.

While we use the same names for neurons in the coiling models as in the swimming models, these names are used to designate the neurons' general projection pattern and neurotransmitter phenotype. Several populations of molecularly defined spinal neurons have been studied in the context of swimming and they served as a basis for our neuron models in the beat-and-glide model. In our model, V2a neurons are modeled as IEDs. IEDs were considered the main source of rhythmogenesis in these spinal locomotor networks based on previous studies showing the necessity and sufficiency of V2a neurons to swimming activity (Eklof-Ljunggren et al., 2012; Ljunggren et al., 2014). However, commissural interneurons were required to ensure repetitive left-right alternation during episodes. Similar to their roles in the generation of double coils, CENs and CINs triggered contralateral tail beats and prevented the premature initiation of contralateral tail beats, respectively. However, the roles of these commissural INs resulted from their projection to contralateral IEDs as opposed to their contralateral projections to PMs in the double coiling model.

In the swimming model, IED formed chemical synapses with caudal IED and CENs, CINs and MNs (the $i^{th}$ IED projected to all caudal CENs, CINs, IEDs, and MNs between the *i+1* and *i+6* segments). Connections between IEDs and IEDs, CINs and MNs were based on experimentally reported connections from V2a neurons to V2a neurons (Ampatzis et al., 2014; Menelaou & McLean, 2019; Song et al., 2020), V2a neurons to V0d neurons (Menelaou & McLean, 2019), and V2a neurons to MNs (Ampatzis et al., 2014; Menelaou & McLean, 2019; Song et al., 2020). A subtype of V2a neurons that project to MNs was shown to bifurcate and have short ascending branches (Menelaou & McLean, 2019), which we modelled (the $i^{th}$ IED projected to rostral CENs and MNs in the *i-1* and *i-2* segments).

Commissural inhibitory CoBL neurons (including neurons from the dI6 and V0d populations) have been shown to be active during swimming (Liao & Fetcho, 2008; Satou et al., 2020). We modelled CoBL neurons as CINs. CINs projected glycinergic synapses to contralateral CINs, IEDs and MNs to provide reciprocal inhibition between sides and to prevent left-right co-contraction. These connections were partly based upon the presence of glycinergic synaptic bursts observed in biological homologs of IEDs and MNs during the coiling stages (Knogler et al., 2014; Saint-Amant & Drapeau, 2000). Also, CoBL neurons have been shown to project to CINs and unidentified ipsilateral descending spinal neurons that could be CiDs, the biological homologs of IEDs (Satou et al., 2020). We modelled the projection pattern of CINs based on the bifurcating axons with short ascending and long descending branches of a subset of neurons in the dI6 subpopulation (Satou et al., 2020). These neurons were shown to be active during swimming. Thus, the $i^{th}$ CINs projected ascending branches to their rostral targets in the *i-1*th segment and projected descending branches to their caudal targets between the *i+1* and *i+6* segments.

Less is known about the connection patterns of commissural excitatory neurons at larval stages. However, in adult zebrafish, V0v commissural excitatory neurons have been shown to have bifurcating axons with shorter ascending branches and longer descending branches (Björnfors & El Manira, 2016). We modelled CENs to project only to contralateral IEDs. The $i^{th}$ CENs projected ascending branches to their rostral targets in the $i\text{-}1^{th}$ segment and projected descending branches to their caudal targets between the *i+1* and *i+6* segments.

We added a last set of neurons to the swimming network. Circumferential ascending (CiA) interneurons emerge during the second wave of neurogenesis in the spinal cord (Bernhardt et al., 1990), and they control swimming vigour as seen in experiments where the genetically-identified V1 neurons are ablated (Kimura & Higashijima, 2019). We thus modelled CiAs as a population of tonic spiking neurons with ipsilateral ascending glycinergic projections (termed IIA in the model) and integrated them into the model. We added ten IIAs per side, which is less numerous than their ipsilateral, descending excitatory counterparts, the IEDs. This relatively lower number of IIAs was partly because their distribution started a bit more caudally, around segment 5, due to their ascending projections. We distributed IIAs from segment 5 to the caudal end. In our model, they

project ascending ipsilateral glycinergic synapses with rostral IEDs (Kimura & Higashijima, 2019), CINs and CENs (Sengupta et al., 2021) such that the IIAs in the $i^{th}$ segment project to their rostral targets in the *i-1* to *i-2* segments. The IIA projections were short based upon recent evidence that their projections to motor circuits are constrained to segmental and immediately-neighbouring somites (Sengupta et al., 2021). Reciprocally, IEDs formed new glutamatergic synapses with caudally located IIA.

Finally, IEDs received tonic motor commands to test whether the rhythm and pattern of swimming could be generated solely from the activity of spinal circuits. The amplitude of the tonic motor commands was decreased with a linear descending rostrocaudal gradient to counterbalance the predominant descending direction of excitation by the descending projections of IEDs and CENs. The $i^{th}$ IED out of a total of $n_{IED}$ IED neurons received a command that was scaled by $(n_{IED}-i)/n_{IED}$. The most rostral IED had an index $i$ of 0 while the most caudal IED had an index of $n_{IED}$ - 1.

Most spinal neurons at larval stages exhibit either tonic firing or firing with spike rate adaptation (Kimura & Higashijima, 2019; Menelaou & McLean, 2012; Menelaou & McLean, 2019; Satou et al., 2020) with a subset of motoneurons showing intrinsic burst firing (Menelaou & McLean, 2012). Therefore, we posited that the generation of rhythmic tail beats was not dependent upon the presence of intrinsically bursting neurons. Almost all of the neurons in the beat-and-glide swimming model were modelled to fire tonically (Fig. 4*B*). However, we could not produce swimming activity that paused for tens to hundreds of milliseconds without at least one neuron that exhibited firing rate deceleration. Therefore, CENs were modelled to exhibit a more chattering or bursting firing pattern (Fig. 4*B*). Unlike coiling generated by PMs that could generate long bursts of spiking lasting hundreds of milliseconds, the burst firing patterns of CENs were much shorter to accommodate the higher frequency of tail beats than coiling movements.

SIMULATION RESULTS The beat-and-glide swimming model exhibited short-duration (hundreds of milliseconds) swimming episodes with left-right alternation (Fig. 4*C, D, F, Supp. Data video S7*). The amplitude of tail beats was smaller than in coiling movements. The tail beat rhythm was at the low end of the 20-40 Hz range (Fig. 4*E*).

To investigate the role of specific neurons in the model's swimming activity, we performed simulations where we silenced the neurons after 5,000 ms by removing their synaptic inputs and then restored their synaptic inputs after another 5,000 ms. Removing synaptic inputs to IEDs completely stopped the generation of tail beats (Fig. 5*A, Supp. Data video S8*), underscoring their primacy to the generation of tail beats as suggested by studies investigating the role of their biological homologs, the CiDs or V2a interneurons (Eklof-Ljunggren et al., 2012; Ljunggren et al., 2014). Silencing another source of excitation in the form of commissural excitation mediated by CENs seemed to be very important in maintaining the beat-and-glide pattern. Silencing CENs did not disrupt rhythmic firing of IEDs or MNs but severely reduced episode duration and the

number of tail beats generated in each episode (Fig. 5*B, Supp. Data video S9*). These simulations suggest that commissural excitation is necessary to activate the silent contralateral side during ongoing swimming to ensure successive left-right alternating tail beats (Björnfors & El Manira, 2016; Saint-Amant, 2010).

Genetic ablation of V1 interneurons, a population of ipsilaterally ascending spinal inhibitory neurons, increased swim vigour but produced no overt changes in swimming pattern (Kimura and Higashijima 2019). Consistent with those experimental results, simulating the removal of ipsilateral ascending inhibition by silencing IIA interneurons seemed to increase the amplitude of motoneuron activity (Fig. 6*A, Supp. Data video S10*). There was a slight increase in the duration of episodes, but the overall beat-and-glide pattern persisted. Left-right alternation was affected in these simulations and during simulations where CINs were silenced (Fig. 6*B, Supp. Data video S11*). These latter simulations replicate the phenotype observed after genetic ablation of a commissural inhibitory subpopulation of dI6 interneurons (Satou et al., 2020). Effects on episode and inter-episode duration were modest or negligible in both simulations where IIA or CINs were silenced.

Since some V2a interneurons in adult zebrafish display pacemaker capacities (Song et al., 2020), we tested whether we could also generate beat-and-glide swimming in a model with bursting IED (Fig. 7*A, Supp. Data video S12*). Decreasing the strength of synapses from IEDs to other neurons and increasing the connection strength of CENs and CINs to contralateral IEDs (**Table 3**) led to 100-400 ms swimming episodes of left-right alternating tail beats at frequencies around 20 Hz (Fig. 7*B-D*). On the other hand, models with only tonic firing neurons failed to generate the hallmarks of beat-and-glide swimming. These models could only generate either short swimming episodes (1-3 tail beats with total episode duration less than 150 ms) that involved more caudal (caudal 60%) parts of the fish or very long (> 1 s) sustained swimming episodes. Fig. 7*E-F (Supp. Data video S13*) illustrates a simulation where swimming behaviour toggled between the short swimming episodes involving only the caudal parts of the fish and the long sustained swimming episodes. Adjusting the synaptic weights or the amplitude of the motor command drive in this last model resulted in swimming characterized uniquely by short swimming episodes or long sustained swimming episodes. The sum of these two simulations and our base beat-and-glide model suggests that burst firing in at least one element of the spinal network is necessary to create beat-and-glide swimming resembling that seen in larval zebrafish.

Previous experimental results showed that at later stages of development, strychnine application disturbed swimming in the 20-40 Hz range (Roussel et al., 2020). Our model's behaviour to loss of glycinergic transmission was tested (Fig. 8*A, Supp. Data video S14*). Motor output was increased when glycinergic transmission was removed (Fig. 8*B*), while the overall episodic pattern of beat-and-glide swimming did not seem to be altered (Fig. 8*C-D*). The frequency content at all body positions became more dispersed in the 0-100 Hz range suggesting that rhythmogenesis is

impaired (Fig. 8*E*). Left-right alternation disappeared and was replaced by broad synchronous activity (Fig. 8*F*). These results indicate that removing glycinergic transmission in the model disrupted the ability to generate left-right alternating tail beats in the 20-40 Hz range typically characteristic of swimming in larval zebrafish.

The sensitivity of the base model to variability was tested by running sets of ten 10-s long simulations at various values of $\sigma_d$, $\sigma_p$ and $\sigma_w$. The episode duration, inter-episode interval, time delay at which the peak of the autocorrelation of muscle output occurred as an estimate of the tail beat period, and the minimum coefficient of the cross-correlation of the left and right muscle output were analyzed (Figs. 9 and 10). To compare the output of the simulations with added noise to the output of the base model, we performed a single 100-s long simulation of the base model that was segmented into ten 10-s long epochs and analyzed. Increases in variability in the motor command drive ($\sigma_d$) seemed to affect episode duration and inter-episode intervals but not tail beat frequency and left-right alternation (Fig. 9*A-D*). On the other hand, variability in synaptic weights ($\sigma_w$) affected left-right alternation as well as episode duration (Fig. 9*E-H*). Small amounts of variability in the parameters shaping the membrane potential dynamics ($\sigma_p$) disrupted the beat-and-glide pattern (Fig. 10*A,B*). As $\sigma_p$ was increased, the rhythm of tail beats and left-right alternation was also disrupted (Fig. 10*C,D*). Even slight variability in the parameters shaping membrane potential dynamics (e.g. $\sigma_p$ = 0.01) resulted in changes in membrane excitability and, in some cases, firing patterns as evidenced by the conversion of some CENs from burst to tonic firing (Fig. 10*E*). Thus, the beat-and-glide model was susceptible to variations in the parameters determining membrane potential dynamics and less to variations in the amplitude of the motor command drive and the synaptic weights as seen in both coiling models.

## DISCUSSION

To our knowledge, this study presents one of the first models of spinal locomotor circuits in developing zebrafish. We have iteratively built several spinal locomotor circuit models that generate locomotor behaviours of the developing zebrafish. These models support mechanisms of network operation of developing zebrafish spinal locomotor circuits described experimentally. Our model suggests that the circuitry driving locomotor movements could switch from a pacemaker kernel located rostrally during coiling movements to network-based spinal circuits during swimming. Results from simulations where select populations of spinal neurons are silenced were consistent with experimental studies. Our sensitivity analysis suggests that the correct operation of spinal circuits for locomotion are not immune to large variations in synaptic weighting and firing behaviours.

### *PM-based network for early simple behaviours*

The earliest locomotor behaviours in zebrafish, namely single and multiple coilings, require global recruitments of neurons to synchronously contract all ipsilateral muscles (Warp et al., 2012). Electrical coupling, which lacks the delays inherent with chemical neurotransmission, enables

these types of ballistic movements. Early locomotor behaviour in zebrafish seems to rely on this architecture, as demonstrated by the necessity of electrical but not chemical synapses (Saint-Amant & Drapeau, 2000, 2001). The rapid and multidirectional current transmission supported by electrical synapses is a perfect solution for en masse activation of a neural circuit (Bennett & Zukin, 2004). However, synchronous activation of an ensemble of neurons does not accommodate rhythmic activity, which requires more precise timing and connection strength. For example, the emergence of double coiling in our model was generated by synaptic excitation of contralateral pacemaker neurons that had to be delayed sufficiently long to enable the first of the coil to complete before initiating the second contralateral coil. Commissural glycinergic transmission was also required to tamper down coiling events with more than two successive coils. If multiple coiling is a preparatory stage towards the emergence of repetitive, left-right alternating tail beats, then the possible importance of contralateral excitation and inhibition at this stage presages the establishment of similar operational mechanisms to the generation of swimming.

*Network oscillator for more refined movements*

To generate swimming, we delegated the generation of the rhythm driving tail beats to network oscillators distributed along the length of the spinal cord. Spinal locomotor circuits may transition away from pacemakers as the source of the rhythm to prevent being vulnerable to any flaws in the function of a small population of neurons. Also, there may be multiple local rhythms that control body oscillations along the developing zebrafish's length. Indeed, locomotor output has proven to be very robust to sectioning of the spinal cord, leading to the suggestion that redundant rhythm-generating circuits must be present within the spinal cord (McDearmid & Drapeau, 2006; Wiggin et al., 2012; Wiggin et al., 2014). Experimental evidence from our lab further suggests that some element of the development of local network oscillators occurs progressively from the caudal toward the rostral end of the body (Roussel et al., 2020).

The CiDs or V2a interneurons, the biological homologs of IEDs, are well recognized as the neural engine that drives swimming activity in zebrafish spinal circuits (Eklof-Ljunggren et al., 2012; Ljunggren et al., 2014). While some V2a interneurons have shown intrinsic burst firing in the adult (Song et al., 2020), V2a interneurons in developing zebrafish show either tonic or modestly spike adapting firing (Menelaou & McLean, 2019). We thus sought to generate beat-and-glide swimming with tonically firing IEDs. Successive left-right alternating tail beats were generated by combining contralateral excitation from bursting commissural excitatory neurons to initiate alternating tail beats and contralateral inhibition to prevent co-contraction of both sides. If tonically firing V2a interneurons drive swimming activity in larval zebrafish, then their central role depends less on their ability to produce any type of bursting rhythm. Instead, the pivotal role of V2a interneurons in enabling swimming activity would be to coordinate the many spinal interneuron populations that generate the patterns of repetitive, left-right alternating tail beats seen in developing zebrafish swimming (Saint-Amant, 2010).

The prominent role of contralateral excitation in ensuring continued left-right alternating tail beats by initiating the activation of the silent side during each tail beat has yet to be tested experimentally. The generation of double coilings also rested upon contralateral excitation of pacemaker neurons and would suggest a conserved mechanism of operation in these two forms of locomotion in developing zebrafish. It is not clear whether a single population of commissural excitation neurons mediates the initiation of a movement on the silent side in both coiling and swimming. It is likely that two different populations are involved as the target of contralateral excitation changed from PMs (in coiling) to IEDs (in swimming).

In the beat-and-glide models with tonically firing IEDs, CENs with burst firings were necessary to generate the appropriate swimming pattern. Otherwise, the model with all tonic neurons could not generate intermittent swim episodes lasting several hundreds of milliseconds. Whether CENs exhibit burst firing in larval zebrafish is unknown and may be unnecessary if V2a neurons can produce burst firing during swimming. As stated above, intracellular recordings of V2a neurons suggest that they are primarily tonic firing or modestly spike adapting firing (Menelaou & McLean, 2019). However, neuromodulators such as serotonin or dopamine could shift their firing activity towards burst firing by upregulating pacemaking promoting currents such as persistent sodium currents (Song et al., 2020).

An analysis of the models' sensitivity to variability in its parameters highlighted the importance of constraining the membrane dynamics that shape the firing behaviour of spinal neurons in particular. This importance has also been observed in other swimming networks (Kozlov et al., 2014; Sautois et al., 2007). Because we used an approach described by Izhekevich (2007) to model the membrane potential dynamics with a small set of differential equations, this model cannot test the contribution of specific ionic currents. While many combinations of ionic currents can generate similar firing behaviours (Goldman et al., 2001), some currents have been identified as being important for locomotor circuits of zebrafish (Song et al., 2020) and other rhythm-generating circuits (e.g. Anderson et al. 2012; Golowasch and Marder 1992; Tazerart et al. 2007; Zhong et al. 2007).

We also tested several hypotheses concerning the role of inhibitory neurons in spinal locomotor networks. The silencing simulations confirmed experimental data suggesting contralateral inhibition reinforces left-right alternation (Satou et al., 2020). In our model, ipsilaterally projecting inhibitory neurons (IIAs) did not play critical roles in rhythmogenesis or pattern formation. Instead, the silencing of this cell type reduced motor output. This is consistent with the effects of silencing Engrailed-1 expressing V1 interneurons, which dampens the activity of slow-swimming motoneurons (Kimura & Higashijima, 2019). Our model generates swimming at the slower range of speeds observed in larval zebrafish. It will be interesting to see whether models able to generate faster swimming speeds will also observe a preferential involvement of V1 interneurons to slower swimming speeds.

To the best of our knowledge, this is the first model to generate several forms of locomotor movements in developing zebrafish based upon previously described neurons and their connectivity patterns. This model could serve as a base model to study more refined control of locomotion in maturing zebrafish, particularly through the involvement of more populations of spinal neurons. For example, the control of swimming vigour and speed would require integrating ipsilaterally projecting V1 interneurons (Kimura & Higashijima, 2019) and V2b population (Callahan et al., 2019) that are likely to be part of the morphologically-defined CiA and VeLD populations, respectively.

In addition, there is increasing evidence that connectivity between subgroups within a population (Menelaou & McLean, 2019; Song et al., 2020) and subgroups belonging to different spinal populations are highly specific (Ampatzis et al., 2014; Bagnall & McLean, 2014; Menelaou & McLean, 2019; Song et al., 2020). This has been demonstrated especially in the context of the modular organization controlling different speeds of locomotion (Ampatzis et al., 2014; Menelaou & McLean, 2012; Song et al., 2020). Indeed, previous studies in zebrafish have shown that MNs and V2a neurons are organized in three different modules (slow, medium and fast) that are differentially recruited according to the swimming speed (Ampatzis et al., 2014; Song et al., 2020). Future iterations of the model could, therefore, differentiate populations of primary and secondary MNs known to be involved in swimming episodes of different speeds (Ampatzis et al., 2013; Menelaou & McLean, 2012) and model the specific connectivity between MNs and V2a populations belonging to the various speed modules (Song et al. 2020). Speed modularity could also be applied to several other spinal neuron classes in the model, including commissural excitatory V0v interneurons (Björnfors & El Manira, 2016; McLean et al., 2008) and commissural inhibitory interneurons belonging to either the dI6 or V0d populations (Satou et al., 2020). This expanded model could then be used to test whether variations in intrinsic properties (Menelaou & McLean, 2012; Song et al., 2018) and specific connectivity patterns within and between modules (Ampatzis et al., 2014; Bagnall & McLean, 2014; Kimura & Higashijima, 2019; Menelaou & McLean, 2019; Song et al., 2020) are important for the speed-dependent recruitment patterns observed during changes in speed (McLean & Fetcho, 2009; McLean et al., 2007, 2008).

By iteratively building upon our model to simulate developmental milestones of the zebrafish locomotor behaviour, we highlight several possible mechanisms of operation that are conserved during the maturation of locomotor movements: 1. The transfer of rhythm generation from a pacemaker kernel (IC neurons) during coiling to more spinal network oscillators centered on V2a neurons acting as the coordinating hub during swimming movements. 2. The role of contralateral excitation in initiating the next movement on the silent side (Björnfors & El Manira, 2016). 3. The importance of intrinsic properties influencing firing behaviour and of synaptic weighting in ensuring the sequence of activity needed for rhythmic tail beats in zebrafish. The models presented herein offer invaluable tools to further investigate the mechanisms by which spinal circuits control

facets of swimming, including speed, direction and intensity through interactions within the spinal cord and with supraspinal command centres.

## MATERIALS AND METHODS

### *Modelling environment*

Modelling was performed using Python 3.6.3 64-bits. We did not analyze the early parts of simulations (up to 200 ms) to allow the effects of initial conditions to dissipate.

### *Modelling of single neurons*

We modelled neurons using a single compartment, simple spiking neuron model developed by Izhikevich (2007). The following general differential equations govern the dynamics of the membrane potential:

$$CV' = k(V - V_r)(V - V_t) - u + I_{syn},$$
$$u' = a(b(V - V_r) - u), \qquad (1)$$
$$if\ \ V = V_{max}, then\ V \leftarrow c, u \leftarrow u + d$$

Specific active conductances are not included in these models. Instead, values of the parameters *a*, *b*, *c*, *d*, and $V_{max}$ (which respectively represent the time scale of the recovery variable *u*, the sensitivity of *u* to the sub-threshold variation of *V*, the reset value of *V* after a spike, the reset value of *u* and the action potential peak), as well as values of the parameters *k*, *C*, $V_r$ and $V_t$ (coefficient for the approximation of the subthreshold part of the fast component of the I-V relation, cell capacitance, resting membrane potential, and threshold of action potential firing) can be selected to model a wide range of firing behaviours including bursting (or chattering) pacemaker, tonic spiking, phasic spiking neurons or firing rate adaptation neurons **(Table 1)**. $I_{syn}$ represents the sum of the synaptic and gap junction currents received by the neuron. For all models, the Euler method was used for solving ordinary differential equations.

### *Modelling synapses*

We modelled all electrical synapses (i.e. gap junctions) as ideal resistors following Ohm's Law:

$$I_{gap:pre,post} = V_{pre} G_{pre,post} \qquad (2)$$

With $I_{gap:pre,post}$ the synaptic current flowing to the postsynaptic neuron from the presynaptic neuron through gap junctions and $G_{pre,post}$ the total conductance of gap junctions between the presynaptic and postsynaptic neurons **(Table 2)**.

Synaptic conductances of chemical synapses were modelled as a sum of two exponentials weighted by a synaptic weight based upon the general equation:

$$I_{pre,post} = (V_{post} - E_{rev})(e^{-\frac{t-t_0}{\tau_r}} - e^{-\frac{t-t_0}{\tau_f}})W_{pre,post}\ \ if V_{pre} > V_{thr} \qquad (3)$$

Where $I_{pre,post}$ is the synaptic current received by the postsynaptic neuron from neurotransmitter release by the presynaptic neuron if the presynaptic neuron membrane potential $V_{pre}$ crosses a voltage threshold $V_{thr}$ at the synapse. $V_{post}$ is the membrane potential of the postsynaptic neuron, $E_{rev}$ is the reversal potential, $\tau_r$ and $\tau_f$ are the rise and fall time constants, respectively, $t_0$ is the time at which $V_{pre}$ crossed $V_{thr}$ and $W_{pre,post}$ is the synaptic weight between the presynaptic and postsynaptic neurons (**Table 3**). $I_{pre,post}$ is equal to 0 if $V_{pre}$ is below $V_{thr}$.

We implemented two types of chemical synapses: glutamatergic and glycinergic synapses. The former differs from the latter by the reversal potential values $E_{rev}$ as well as the time constant values $\tau_r$ and $\tau_f$ **(Table 4)**. Values of the glycinergic $E_{rev}$ are depolarized at early developmental stages (Saint-Amant & Drapeau, 2000, 2001), and this reversal potential becomes gradually hyperpolarized (Ben-Ari, 2002). All chemical synapses were turned off in the initial 500 ms of every simulation to allow initial conditions to dissipate.

### *Spatial arrangement of spinal neurons*

A key feature of our modelling approach was to assign spatial coordinates *(x, y)* to point-like neurons (i.e. neurons have no spatial dimension, but they have a position in space), giving the spatial distribution of neurons a central place in our model computing process. We used the Euclidian distance to calculate the distance between each neuron and to approximate axon length. Distance unit is arbitrary and was set so that one model somite was 1.6 arbitrary distance unit (a.d.u.) long. Time delays for each synaptic connection were computed as a function of the distance between neurons and were used to calculate delayed synaptic current:

$$I_{delayed:pre,post}(t) = I_{pre,post}(t - \frac{D_{pre,post}}{cv}) \qquad (4)$$

With $D_{pre,post}$, the Euclidian distance between the presynaptic and postsynaptic neurons and *cv*, the transmission speed. This distance, as well as neuron position, was also used to apply conditions on synaptic weights of neurons (e.g. limits as to how far descending neurons projected to). For the single coiling model, *cv* was set to 0.55 a.d.u/s. For the multiple coiling model, *cv* was set to 1.0 a.d.u/s. These values were obtained through trial-and-error and may reflect changes in myelination and body size of the developing zebrafish. For the beat-and-glide swimming model, *cv* was set to 0.8 a.d.u/s, which led to intersegmental transmission delays in the range of 3.0-4.0 ms, closely matching with the 1.6 ms intersomitic delay previously reported (McDearmid & Drapeau, 2006), assuming that each model segment represents two biological somites at this developmental stage (see *Musculoskeletal model* below).

Spinal locomotor circuits were distributed across two columns, one for each side of the body, giving the network a nearly one-dimensional organization along the rostrocaudal axis. Therefore, we used the *x*-axis as the rostrocaudal axis, whereas the *y*-axis was only used to partition neurons

from the left and right sides (giving the coordinate $y = 1$ a.d.u. for the right side and $y = -1$ a.d.u. for the left side).

### *Sensitivity testing*

We scaled key parameters to Gaussian noise to test the robustness of our three base models (single coiling, multiple coiling, and beat-and-glide swimming) to parameter variability. Sensitivity to noise of the base models was tested by scaling the parameters that set the tonic motor command drive's amplitude, the membrane potential dynamics (Izhikevich model), and synaptic weighting. These three sets of parameters were randomized by multiplying the parameters with a random number picked from a Gaussian distribution with mean, $\mu = 1$, and standard deviations, $\sigma_d$, $\sigma_p$, and $\sigma_w$, respectively. The amplitude of the motor command drive was randomized at each time point. The parameters for the membrane potential dynamics and synaptic weights were randomized at the start of each simulation and did not change during the simulations.

### *Musculoskeletal model*

We implemented a musculoskeletal model of the fish body to convert the output of the spinal circuit model into changes in body angles and frequency of locomotor movements. Each MN output along the fish body was inputted into a muscle cell (Fig. 1*A*,*B*) modelled as a simple passive RC circuit (*R* and *C* being the muscle cell membrane resistance and capacitance, respectively), described by the following equation:

$$V'_{muscle} = \frac{V}{RC} + \frac{I_{syn}}{C} \qquad (5)$$

For muscle cells, values of R were 25 (single coiling), 50 (double coiling) and 1 (beat-and-glide); values of C were 10 (single coiling), 5 (double coiling) and 3 (beat-and-glide). These values were chosen to produce kinematics representative of those seen experimentally. To reduce computational load, we modelled one muscle cell as representing three somites of the body during coiling, and two somites of the body during swimming. The whole body of the fish was modelled as a chain of uncoupled damped pendulums. We computed local body angles according to the difference in activity between the local left and right somites (i.e. muscle cells). The deflection angle $\theta_i$ of the i$^{th}$ somite was computed according to the following differential equation.

$$\theta_i'' + 2\zeta\omega_0\theta_i' + \omega_0^2\theta_i = \alpha(1 - 0.2R)(V_{Rmuscle,i} - V_{Lmuscle,i}) \qquad (6)$$

With $V_{Rmuscle,i}$ and $V_{Lmuscle,i}$ being the solution of the equation *(5)* for the right and left muscles from the $i^{th}$ somite, respectively (Fig. 1*C*). $\alpha$ is the conversion coefficient from an electric drive of the muscle cells to a mechanical contraction of the same cells. The midline of the body can be computed at any given time as (*x*,*y*) coordinates using trigonometric identities from $\theta_i$(Fig 1*D*). Thus, heat maps of local body angle ($\theta_i$) variation through time provides comprehensive information about the network output (Fig. 1*E*). Fast Fourier Transforms (FFT) of the local body

angles were computed to give a map of the local body bend frequencies. Left-right alternation at a particular somite was analyzed using cross-correlation of the left and right muscle output at that somite.

### *Statistical Analysis*

Statistical analysis was performed using the SciPy Python library. Statistical tests consisted of one-factor ANOVA tests followed by two-tailed Student's t-tests. A p-value $< 0.05$ was used to determine statistical significance, and all tests were corrected for multiple comparisons (Bonferroni correction for multiple t-tests).

### *Availability of code*

The code for the model can be accessed at https://github.com/bui-lab/code (pending acceptance of the manuscript).

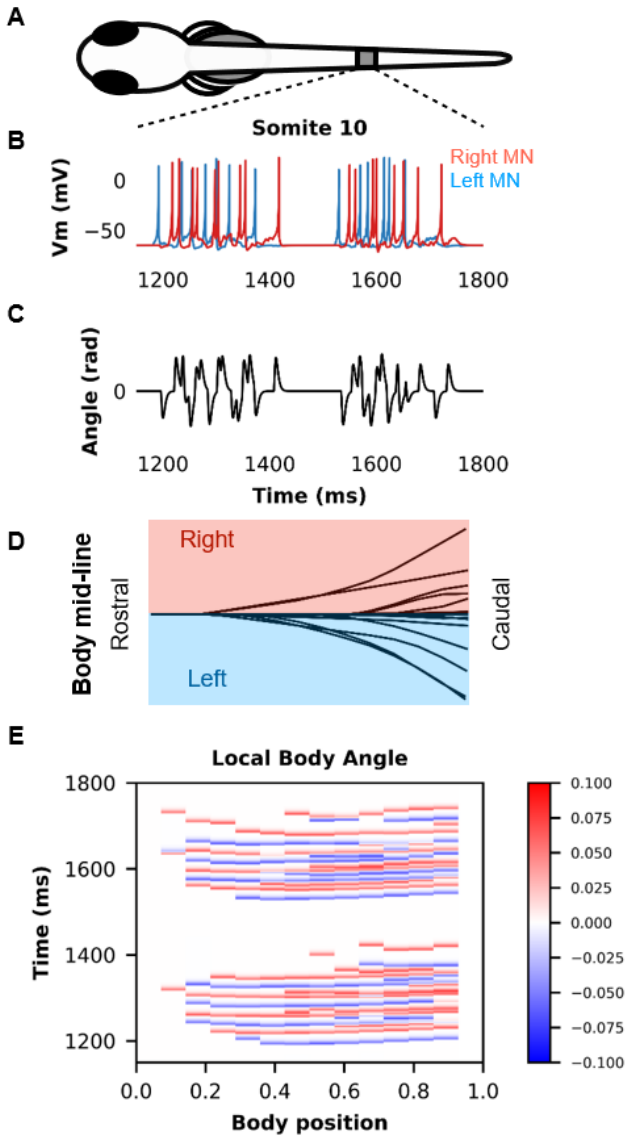


**Figure 1. Simulation of the spinal locomotor network coupled to musculoskeletal model** ***A,*** Schematic of a fish body (Top view). ***B,*** Motoneuron (MNs) output in the 10$^{th}$ somite from a simulated spinal circuit generating beat-and-glide swimming (red trace for the right MN and blue trace for the left MN) is used to calculate body angle variation (***C***) of this segment in a musculoskeletal model. ***D,*** Body midlines extracted from two episodes of beat-and-glide swimming. Body midline is computed by compiling all the calculated local body angles along the simulated fish body. ***E,*** Heat map of local body angle (in radians) across the total body length and through time. Red is for right curvatures while blue labels left curvatures. Body position on the abscissa, 0 is the rostral extremity while 1 is the caudal extremity.

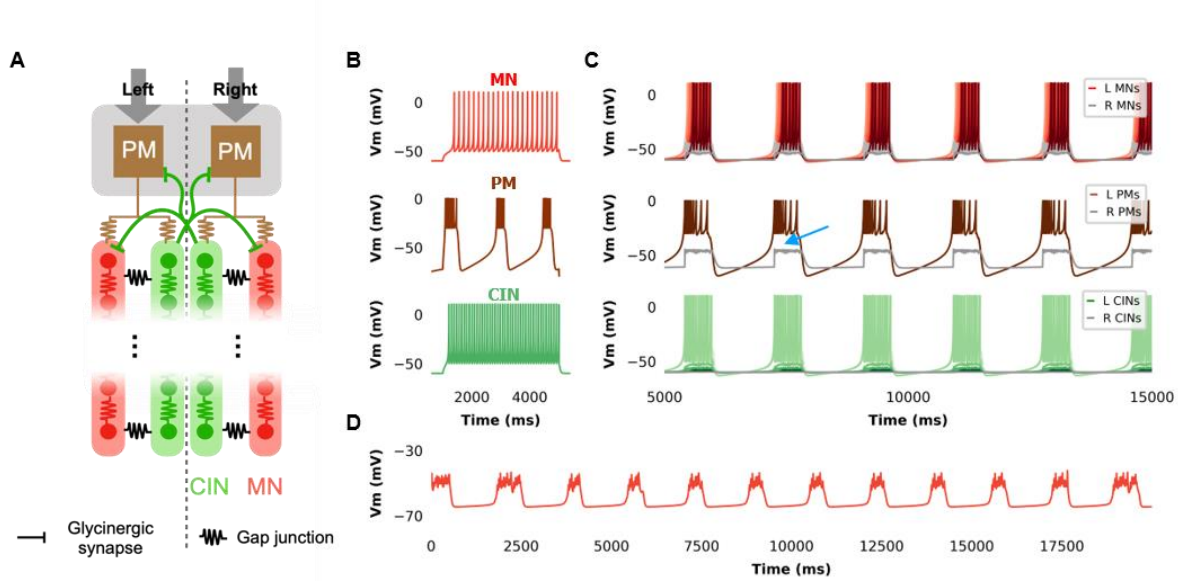


**Figure 2**. **Single coiling model relies on a fully electrical network driven by pacemaker neurons.** ***A***, Schematic of the model architecture underlying single coiling. ***B***, Response to a depolarizing current step of spinal neurons in the model. ***C***, Membrane potential during a simulation with a tonic command to left pacemakers only. Note the synaptic bursts in grey in MNs and PM neurons (a blue arrow marks an example). Lighter and darker colours denote rostral and caudal neurons, respectively. ***D***, Periodic depolarizations in a hyperpolarized motoneuron on the same side where single coilings are generated. Vm: Membrane potential, L: left, R: Right.

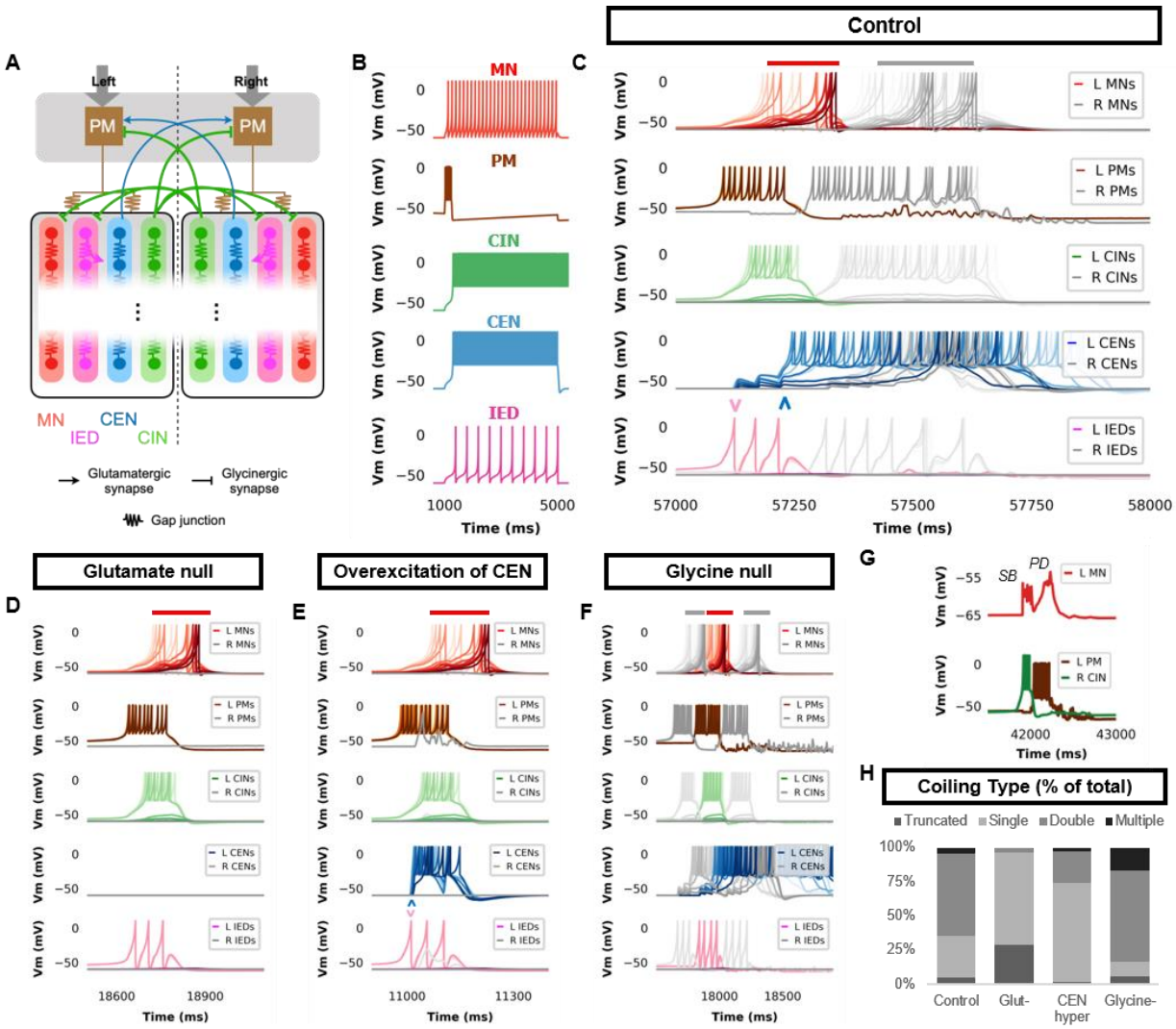


**Figure 3. Double coiling model relies on a hybrid network of electrical and chemical synapses. *A*,** Schematic of the model architecture underlying double coiling. ***B***, Response to a depolarizing current step of spinal neurons in the model. ***C***, Membrane potential during a double coil. Membrane potential in simulations where, ***D***, all glutamatergic transmission was blocked, ***E***, the weights of the IED to CEN and the CEN to PM synapses were increased to show that early excitation of CEN prevented the initiation of a second coil following a single coil, and ***F***, glycinergic transmission was blocked. ***G,*** *Top*, Mixed event composed of a synaptic burst (*SB*) directly followed by a periodic depolarization (*PD*) in a motoneuron. *Bottom*, Membrane potential in left PM and right CIN during the mixed SB-PD event. ***H***, Proportions of single, double, multiple and truncated coiling events under control (Ctrl) conditions, while blocking glutamatergic (Glut$^-$), overexcited CENs (CEN hyper), and blocking glycinergic synapses (Gly$^-$). Solid red and gray bars in *C-F* indicate the duration of coils. Chevrons in *C* and *E* denote the initial spiking of CENs and IEDs to indicate latency of CEN firing during the first coil. For *C-F*, lighter and darker colours denote rostral and caudal neurons, respectively. Vm: Membrane potential, L: left, R: Right.

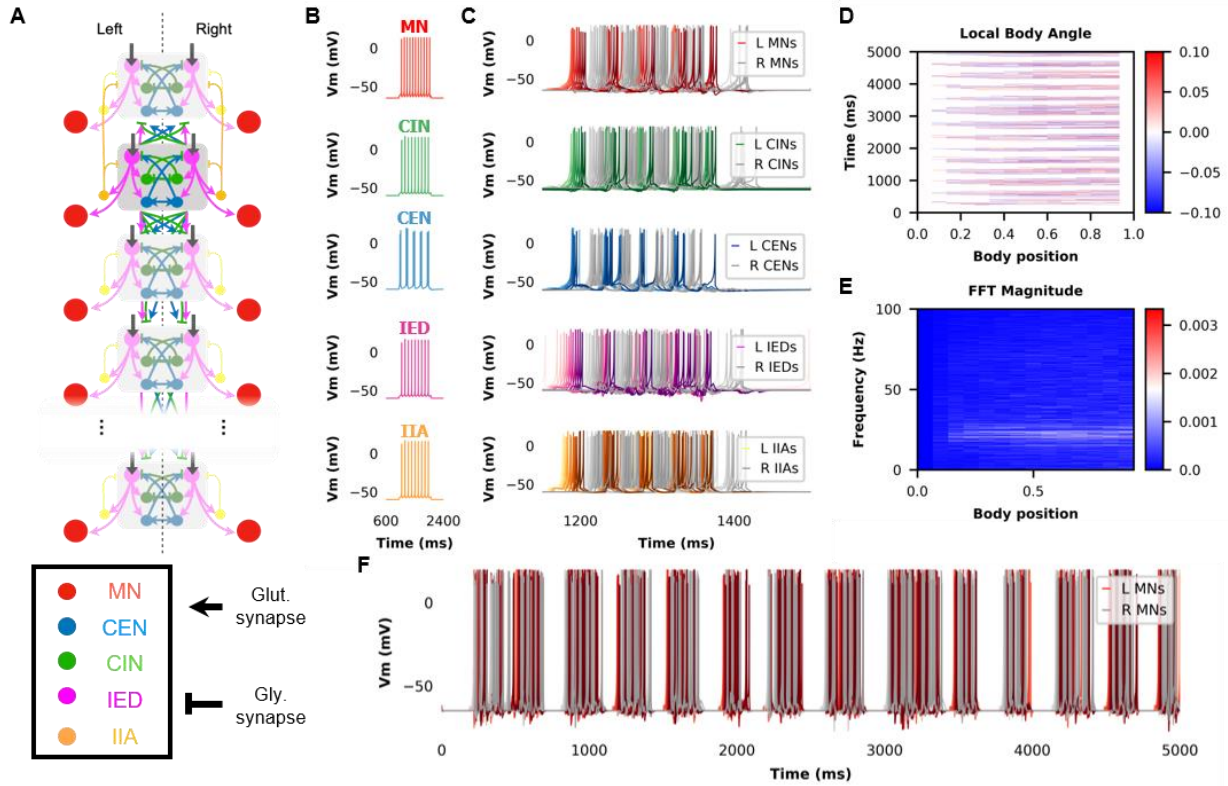


**Figure 4. The base model for beat-and-glide swimming *A*,** Schematic of the model architecture underlying beat-and-glide swimming. ***B*,** Response to a depolarizing current step of spinal neurons in the model. ***C***, Membrane potential during a beat-and-glide swimming simulation with a tonic command to left and right IEDs. ***D*,** Heat-map of local body angle. ***E*,** Fast Fourier Transform (FFT) of local body angle to estimate rhythmicity of tail beats. Most of the power throughout the body is found in the 20 Hz range. ***F***, Motoneuron membrane potential in a 5,000 ms simulation showing a beat-and-glide pattern. For *C* and *F*, lighter and darker colours denote rostral and caudal neurons, respectively. Vm: Membrane potential, L: left, R: Right.

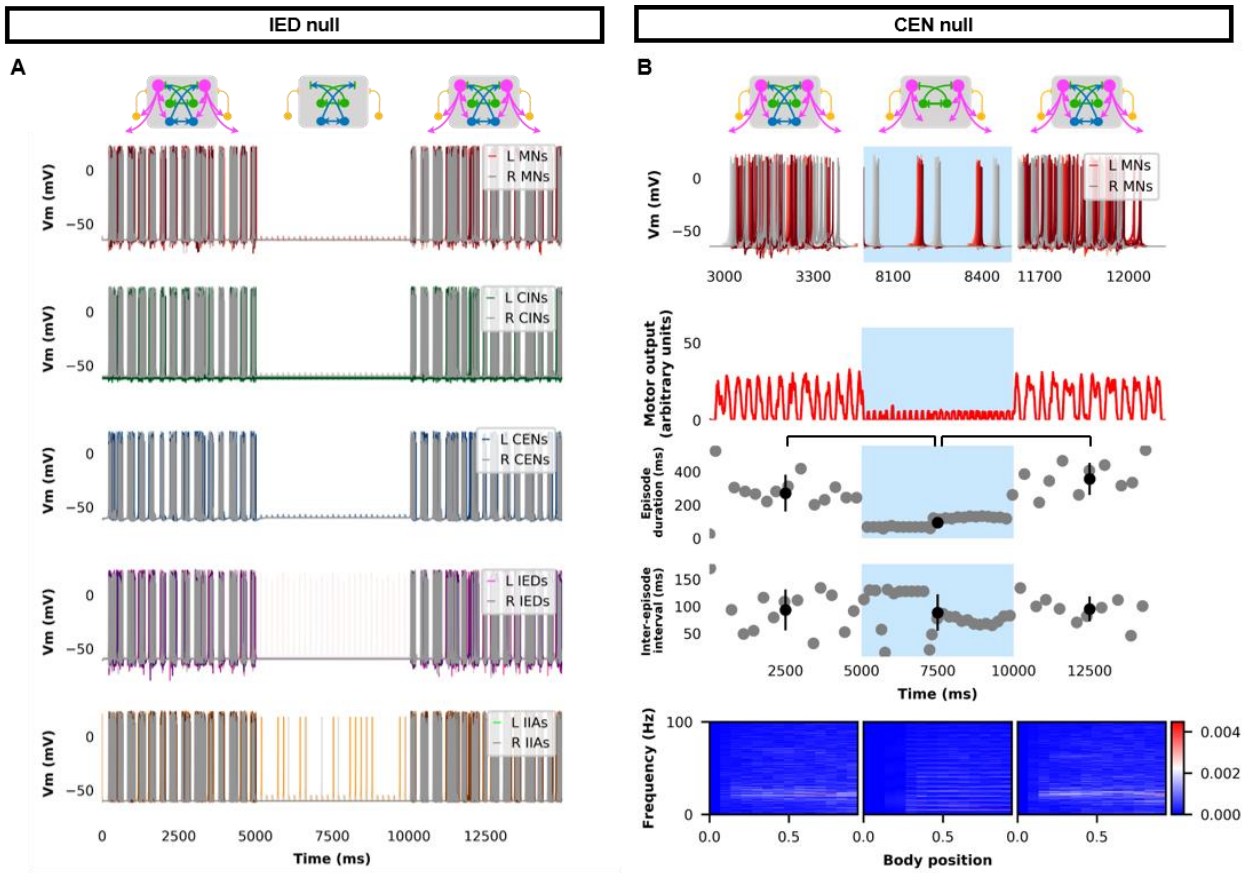


**Figure 5. Reducing the activity of excitatory spinal neurons during beat-and-glide swimming** Simulations to assess the contributions of different spinal neurons consisted of three 5,000 ms epochs. In the middle epoch, silencing of targeted spinal neurons was achieved by removing all synaptic and external currents to the targeted population. Synaptic and external currents were restored in the last epoch. ***A,*** Traces of spinal neurons during simulations where IEDs were silenced in the middle epoch. Swimming activity was eliminated during the middle epoch. ***B,*** Row 1 depicts the functional state of the spinal network during the three epochs. Row 2 shows traces of spinal motoneurons during simulations where CENs were silenced in the middle epoch. Row 3 shows the integrated motor output (sum of left and right motoneuron activity was summed). Rows 4-5 show the episode duration and inter-episode intervals during this simulation. The threshold for estimating the start and end of each episode duration was 0.5 arbitrary units of the integrated motor output. Averages within epoch are shown in black (mean ± s.d.). Brackets denote significant pairwise differences. Row 6 shows the Fast Fourier Transform (FFT) of the local body angle. Lighter and darker colours denote rostral and caudal neurons, respectively. Vm: Membrane potential, L: left, R: Right. ***Statistics***: ***B***, Row 4, one-way ANOVA ($F(2,52) = 54.9$, $p = 2.4 \times 10^{-13}$) followed by two-tailed unpaired Student's t-test (epoch 1 - epoch 2, $p = 1.8 \times 10^{-9}$; epoch 2 - epoch 3, $p = 6.3 \times 10^{-15}$; epoch 1 - epoch 3, $p = 0.06$). Row 5, one-way ANOVA ($F(2,49) = 0.19$, $p = 0.83$).

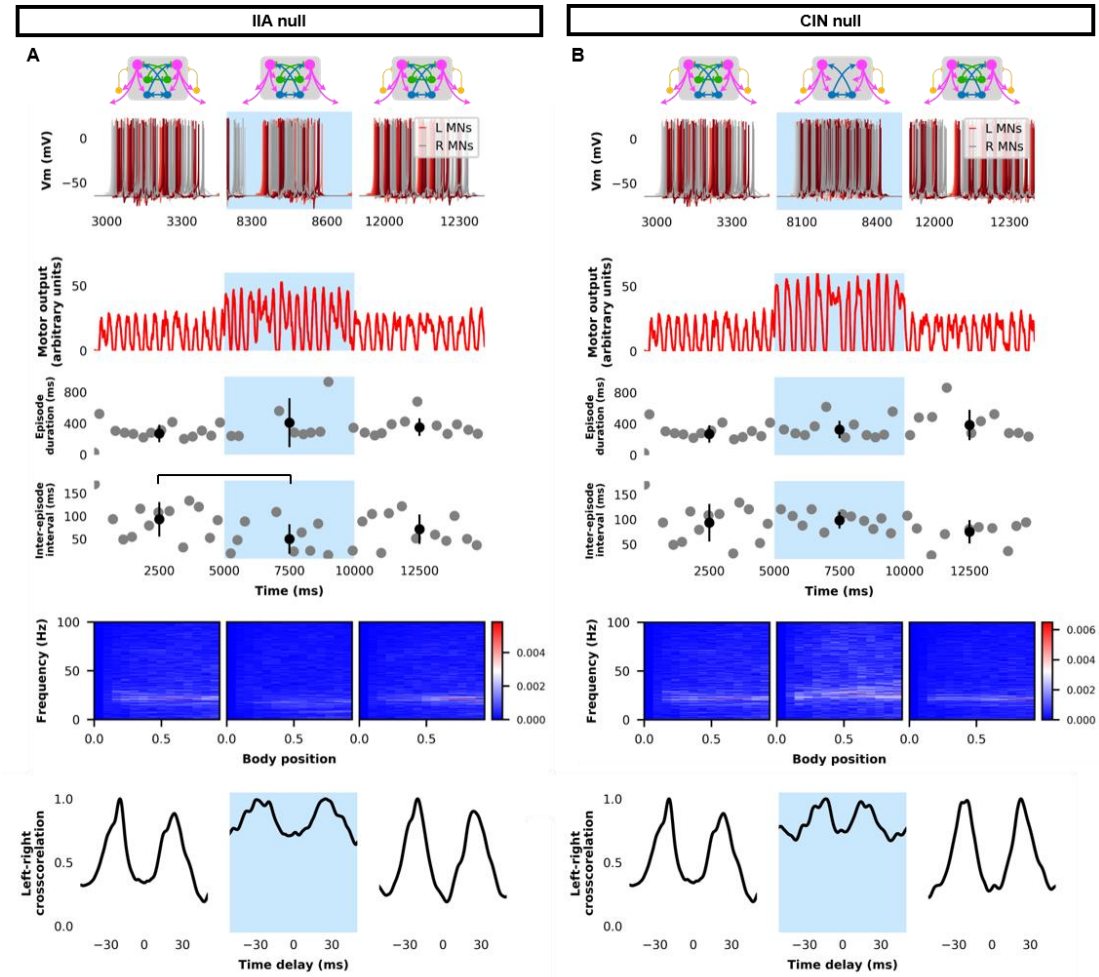


**Figure 6. Reducing the activity of inhibitory spinal neurons during beat-and-glide swimming**
Simulations to assess the contributions of different spinal neurons consisted of three 5,000 ms epochs. In the middle epoch, silencing of targeted spinal neurons was achieved by removing all synaptic and external currents to the targeted population. Synaptic and external currents were restored in the last epoch. Traces of spinal neurons during simulations where ***A,*** IIAs were silenced and ***B***, during simulations where the CINs were silenced in the middle epoch. Row 1 depicts the functional state of the spinal network during the three epochs. Row 2 shows traces of spinal motoneurons during simulations where targeted neurons were silenced in the middle epoch. Row 3 shows the integrated motor output (sum of left and right motoneuron activity was summed). Rows 4-5 show the episode duration and inter-episode intervals during this simulation. The threshold for estimating the start and end of each episode duration was 0.5 arbitrary units of the integrated motor output. Averages within epoch are shown in black (mean ± s.d.). Row 6 shows the FFT of the local body angle. Brackets denote significant pairwise differences. Row 7 shows the left-right coordination of somite 10. Lighter and darker colours denote rostral and caudal neurons, respectively. Vm: Membrane potential, L: left, R: Right. ***Statistics***: ***A***, Row 4, one-way ANOVA ($F(2,36) = 1.48$, $p = 0.24$). Row 5, one-way ANOVA ($F(2,33) = 4.09$, $p = 0.03$) followed by two-tailed unpaired Student's t-test (epoch 1 - epoch 2, $p = 0.01$; epoch 2 - epoch 3, $p = 0.17$; epoch 1 - epoch 3, $p = 0.16$). ***B***, Row 4, one-way ANOVA ($F(2, 36) = 1.90$, $p = 0.17$). Row 5, one-way ANOVA ($F(2, 33) = 1.73$, $p = 0.19$).

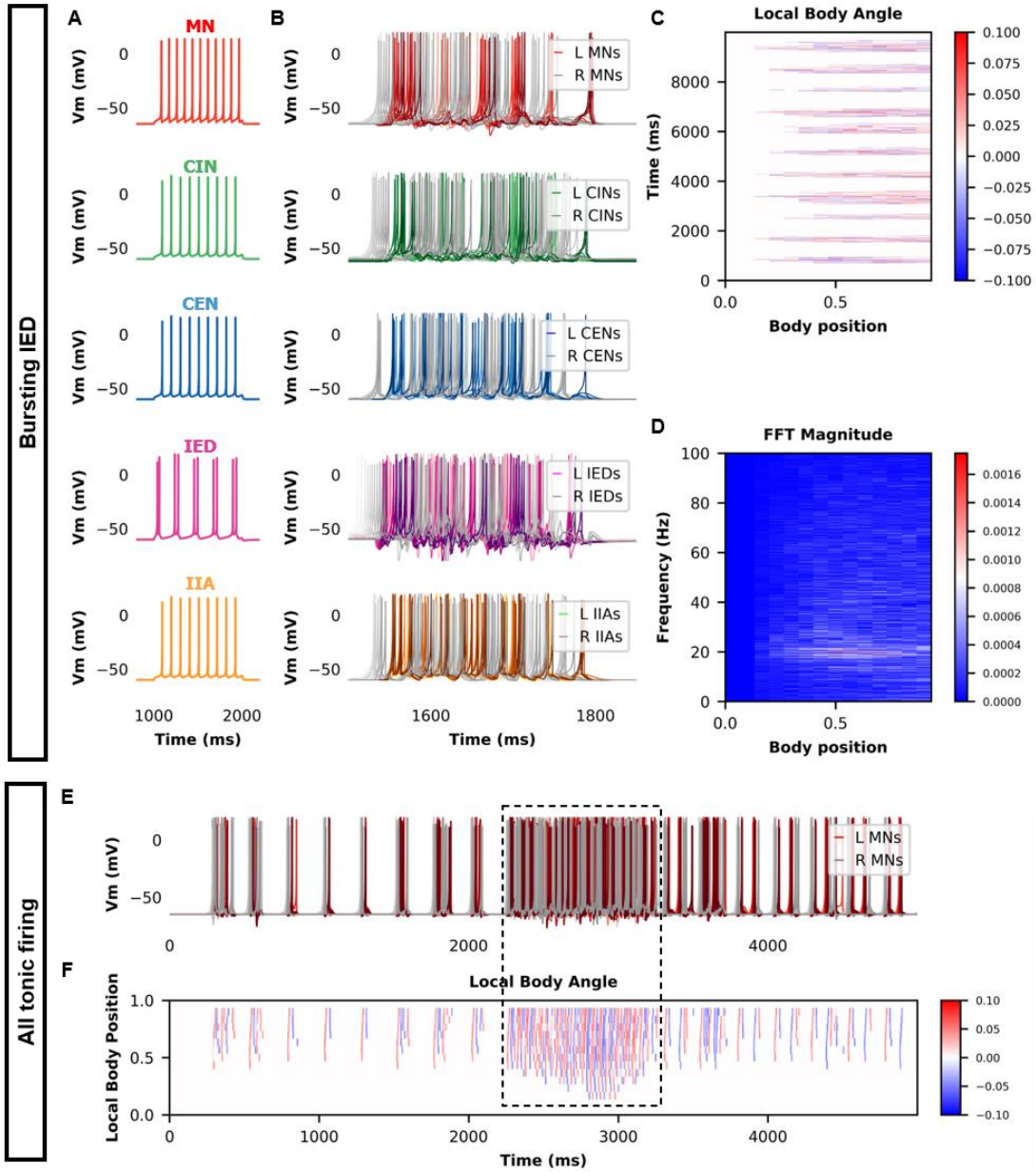


**Figure 7. Beat-and-glide models with bursting IED or only tonic neurons *A***, Response of neurons to a current step. ***B***, Neuron activity during 50 s simulation of beat-and-glide network with bursting IED. ***C***, Heat-map of local body angle. ***D***, Fast Fourier Transform (FFT) of local body angle to estimate rhythmicity of tail beats. ***E***, Motoneuron activity during simulations of beat-and-glide network with just tonic neurons. At this driving command, the model switched between short swimming episodes and a long swimming episode (dashed box). ***F***, Heat-map of local body angle. Note that during short swimming episodes, the tail beats only involve the most caudal 60% of the model. For *B* and *E*, lighter and darker colours denote rostral and caudal neurons, respectively. Vm: Membrane potential, L: left, R: Right.

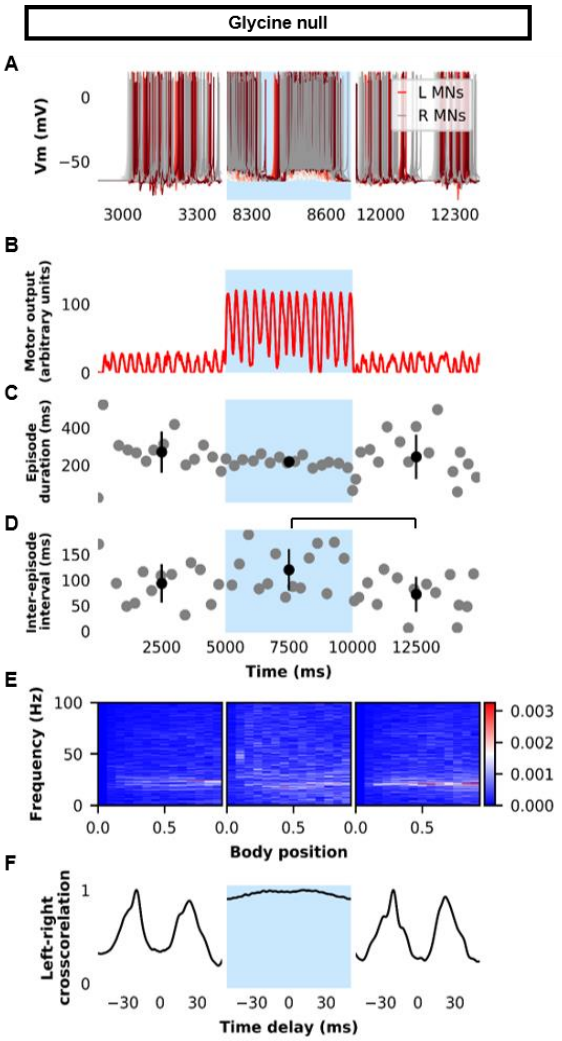


**Figure 8. Simulating the effects of strychnine on beat-and-glide swimming** Simulations to assess the effects of blocking glycinergic transmission consisted of three 5,000 ms epochs. In the middle epoch, blocking glycinergic transmission was achieved by changing all glycinergic synaptic currents to 0. Glycinergic transmission was restored in the last epoch. ***A***, traces of spinal motoneurons during simulations where glycinergic transmission was blocked in the middle epoch. ***B***, the integrated motor output (sum of left and right motoneuron activity was summed). ***C***, the episode duration and ***D***, the inter-episode intervals during this simulation. The threshold to estimate the start and end of each episode duration was 0.5 arbitrary units of the integrated motor output for the first and last epoch, and 50 arbitrary units for the middle epoch due to the greatly increased motor output. Averages within epoch are shown in black (mean ± s.d.). ***E***, the Fast Fourier Transform (FFT) of the local body angle. ***F***, the left-right coordination of somite 10. Brackets denote pairwise significant differences. Lighter and darker colours denote rostral and caudal neurons, respectively. Vm: Membrane potential, L: left, R: Right. ***Statistics***: *C*, one-way ANOVA ($F(2,44) = 1.0$, $p = 0.38$). *D*, one-way ANOVA ($F(2,41) = 5.46$, $p = 0.008$) followed by two-tailed unpaired Student's t-test (epoch 1 - epoch 2, $p = 0.10$; epoch 2 - epoch 3, $p = 0.003$; epoch 1 - epoch 3, $p = 0.15$).

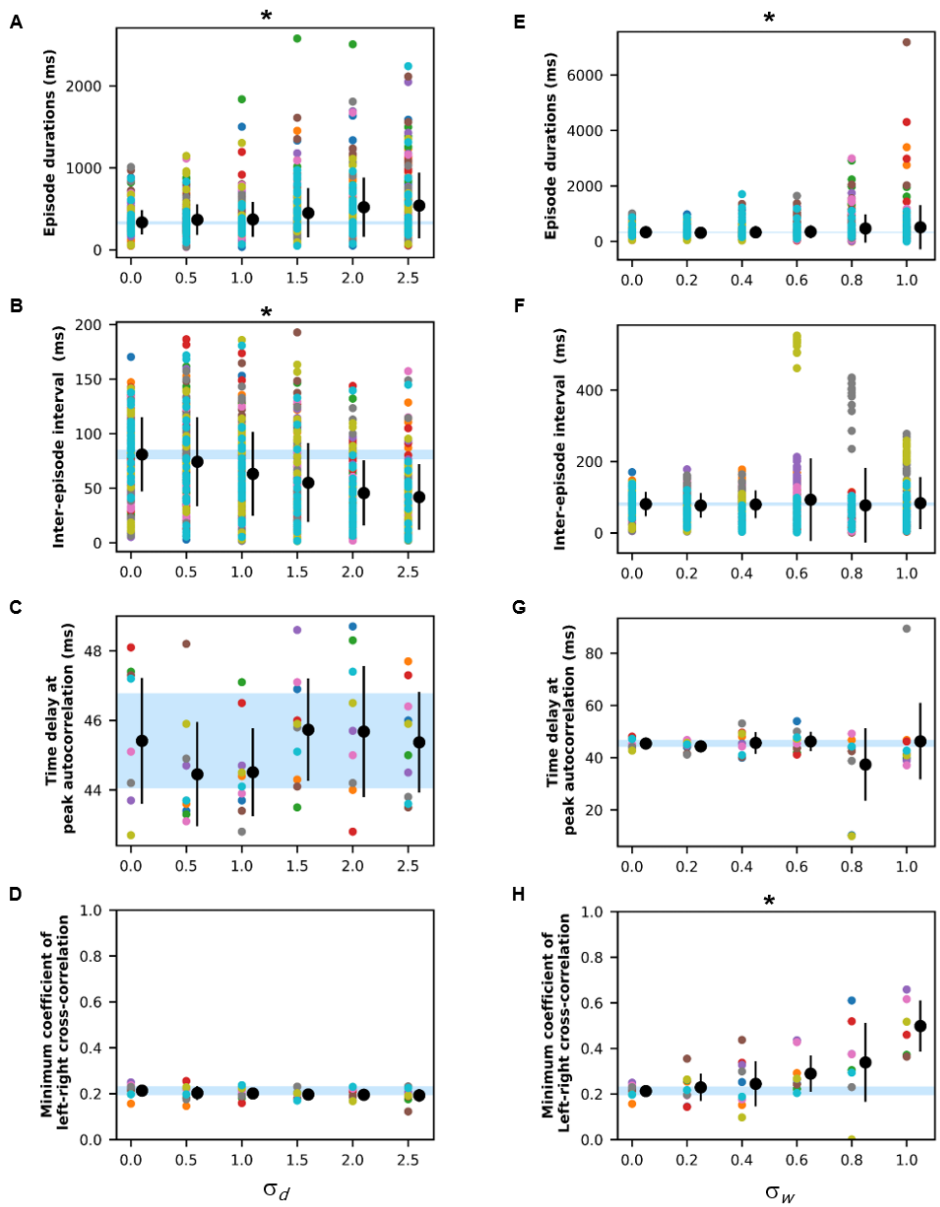


**Figure 9. Sensitivity of beat-and-glide swimming to tonic drive amplitude and synaptic weighting.** Ten 10-s long simulations were run for each values of $\sigma_d$ ***(A-D)*** and $\sigma_w$***(E-H)*** tested***. A, E***: Episode duration. ***B***, ***F***: Inter-episode interval. ***C***, ***G***: Time delay where the peak of the autocorrelation of muscle output occurs in the 20-50 Hz range. ***D***, ***H***: Minimum coefficient of the cross-correlation of left and right muscle**.** The minimum was taken between -10 and 10 ms time delays. Each circle represents a single swimming episode (*A*, *E*), inter-episode interval (*B*, *F*) or a single run (*C*, *D*, *G*, *H*). Colours correspond to values from the same run (*A*, *B*, *E*, *F*) or individual runs (*C*, *D*, *G*, *H*). Runs with only one side showing activity are not depicted in *D* and *H*. Black circles and error bars represent mean and standard deviations, respectively. Horizontal blue bars denote 95% confidence interval of the mean for the base model with no parameter variability ($\sigma_d = \sigma_p = \sigma_w = 0$). Asterisks indicate characteristics with significant difference between the means. ***Statistics***: *A*, one-way ANOVA ($F(5,1228) = 19.6$, $p = 9.1 \times 10^{-19}$). *B*, one-way ANOVA ($F(5,1228) = 38.5$, $p = 7.9 \times 10^{-37}$), *C*, one-way ANOVA ($F(5,54) = 1.17$, $p = 0.33$), *D*, one-way ANOVA ($F(5,54) = 0.77$, $p = 0.58$), *E*, one-way ANOVA ($F(5,1225) = 8.7$, $p = 4.3 \times 10^{-8}$). *F*, one-way ANOVA ($F(5,1225) = 1.43$, $p = 0.21$), *G*, one-way ANOVA ($F(5,54) = 1.42$, $p = 0.23$), *H*, one-way ANOVA ($F(5,47) = 7.24$, $p = 4 \times 10^{-5}$). P-values for t-tests are found in Supplementary Table 1.

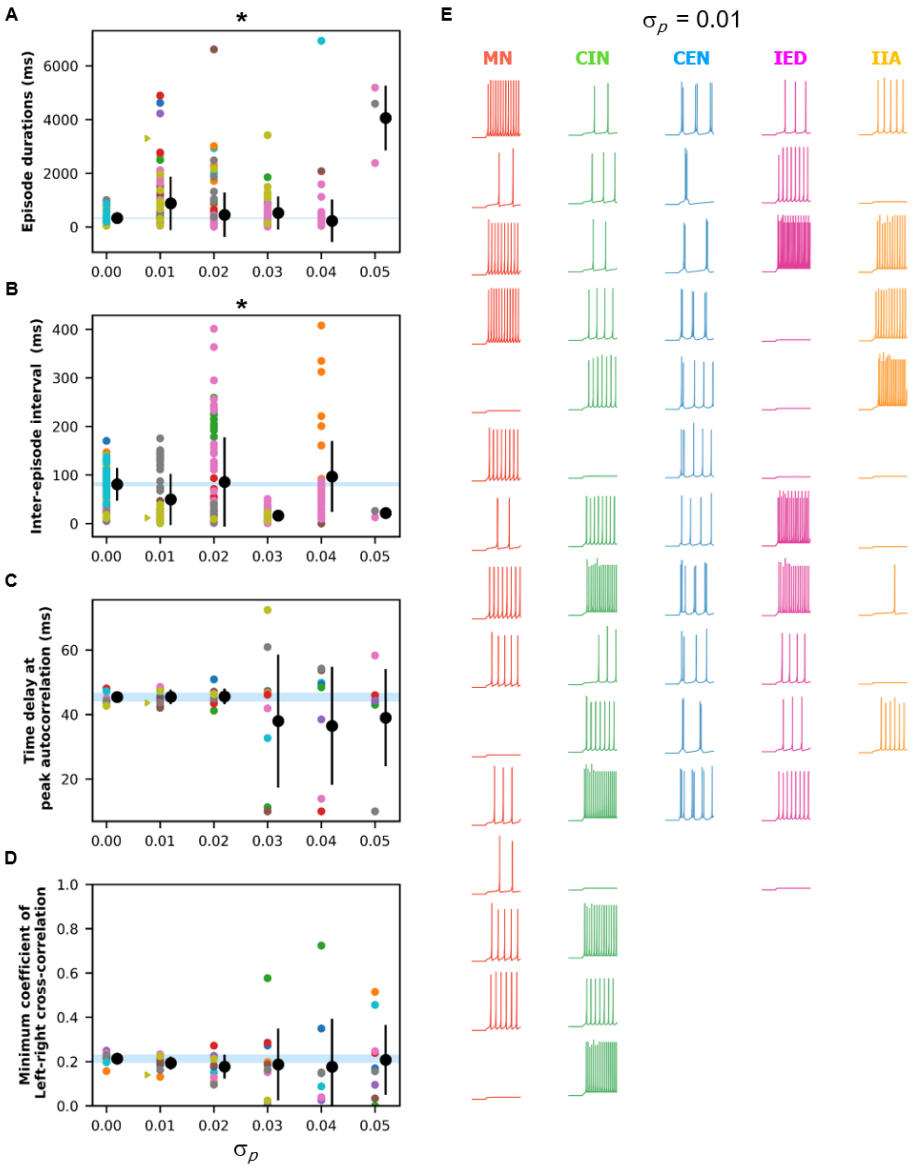


**Figure 10. Sensitivity of beat-and-glide swimming to variability in membrane potential dynamics.** Ten 10-s long simulations were run at each value of $\sigma_p$ **(*A*-*D*). *A*,** Episode duration. ***B***, Inter-episode interval. ***C***, Time delay where the peak of the autocorrelation of muscle output occurs in the 20-50 Hz range. ***D***, Minimum coefficient of the cross-correlation of left and right muscle**.** The minimum was taken between -10 and 10 ms time delays. Each circle represents a single swimming episode (*A*), inter-episode interval (*B*) or a single run (*C*, *D*). Colours correspond to values from the same run (*A*, *B*) or individual runs (*C*, *D*). Black circles and error bars represent mean and standard deviations, respectively. One run at $\sigma_p$= 0.01 and 0.04 exhibited no swimming activity. Teal arrowheads indicate average values for the model further illustrated in *E*. Horizontal blue bars denote 95% confidence interval of the mean for the base model with no parameter variability ($\sigma_d$= $\sigma_p$=$\sigma_w$ = 0). ***E***, Responses to a 1-s long step current of all neurons on the left side in a model where $\sigma_p$= 0.01. Step current amplitude to a population of neurons was the same for each neuron within that population. Step current amplitudes varied between populations of neurons. The amplitude of the step currents to each population is the same as in Fig. 4*B*. Asterisks indicate characteristics with significant difference between the means. ***Statistics***: *A*, one-way ANOVA (F(5,551) = 28.6, p = 7.4 x $10^{-26}$). *B*, one-way ANOVA (F(5,551) = 15.5, p = 2.5 x 1-$^{-14}$), *C*, one-way ANOVA (F(5,52) = 0.94, p = 0.46), *D*, one-way ANOVA (F(5,52) = 0.13, p = 0.98). P-values for t-tests are found in Supplementary Table 2.

**Table 1.** *Parameter values of neurons in coiling models*

| Model Population | Possible biological homologs[1] | Izhikievich parameters | | | | | | | | | Rostro-caudal position[2] | $I_{drive}$[3] |
|---|---|---|---|---|---|---|---|---|---|---|---|---|
| | | ***A*** | ***b*** | ***c*** | ***d*** | $V_{max}$ | $V_r$ | $V_t$ | ***k*** | ***C*** | | |
| MN | pMN | | | | | | | | | | | |
| Single | (coils) | 0.5 | 0.1 | -50 | 0.2 | 10 | -60 | -45 | 0.05 | 20 | 5.0 +1.6*n | |
| Multiple | sMN | 0.5 | 0.1 | -50 | 100 | 10 | -60 | -50 | 0.05 | 20 | | |
| Beat-and-glide | (swim) | 0.5 | 0.01 | -55 | 100 | 10 | -65 | -58 | 0.5 | 20 | | |
| PM | IC | | | - | | | | | | | | |
| Single | | 0.0005 | 0.5 | -30 | 5 | 0 | -60 | -45 | 0.05 | 50 | 1.0 | 50 |
| Multiple | | 0.0002 | 0.5 | -40 | 5 | 0 | -60 | -45 | 0.03 | 50 | | 35 |
| CIN | CoBL | | | | | | | | | | 5.0 +1.6*n | |
| Single | (dI6, | 0.5 | 0.01 | -50 | 0.2 | 10 | -60 | -45 | 0.05 | 20 | | |
| Multiple | V0d), | 0.02 | 0.1 | -30 | 3.75 | 10 | -60 | -45 | 0.09 | 6 | | |
| Beat-and-glide | | 0.1 | 0.002 | -55 | 4 | 10 | -60 | -54 | 0.3 | 10 | | |
| CEN | V0v | | | | | | | | | | 5.1 +1.6*n | |
| Multiple | | 0.02 | 0.1 | -30 | 11.6 | 10 | -60 | -45 | 0.05 | 20 | | |
| Beat-and-glide | | 0.01 | 0.002 | -55 | 8 | 10 | -60 | -54 | 0.3 | 10 | | |
| Beat-and-glide (bursting) | | 0.1 | 0.002 | -55 | 4 | 10 | -60 | -54 | 0.3 | 10 | | |
| IED | CiD | | | | | | | | | | | |
| Multiple | (V2a) | 0.5 | 0.1 | -50 | 100 | 10 | -60 | -45 | 0.05 | 20 | 5.1 | |
| Beat-and-glide | | 0.1 | 0.002 | -55 | 4 | 10 | -60 | -54 | 0.3 | 10 | 8.1 | 3.15 |
| Beat-and-glide (bursting) | | 0.01 | 0.002 | -55 | 2 | 8 | -60 | -54 | 0.3 | 10 | +1.6*n | |
| IIA | CiA (V1) | | | | | | | | | | | |
| Beat-and-glide | | 0.1 | 0.002 | -55 | 4 | 10 | -60 | -54 | 0.3 | 10 | 10.1 +1.6*n | |

[1] *Candidate population based upon morphological characterization. Genetically-identified populations that comprise the morphologically defined populations in parentheses.*

[2] *n = 0 to N-1, N being the total number of neurons in that given population.*

[3] *Amplitude of tonic motor command drive used in the base models.*

**Table 2.** *Electrical synapse (gap junctions) weights between neuron populations.*

| Population | MN | PM | CIN | CEN | IED | IIA |
|---|---|---|---|---|---|---|
| **MN** | | | | | | |
| Single-coiling | 0.1 | - | - | - | - | - |
| Double-coiling | 0.07 | | | | | |
| Beat-and-glide | 0.005 | | | | | |
| **PM** | | | | | | |
| Single-coiling | 0.04 | 0.001 | - | - | - | - |
| Double-coiling | 0.03 | 0.0001 | | | | |
| **CIN** | | | | | | |
| Single-coiling | 0.01 | 0.05 | 0.04 | - | - | - |
| Double-coiling | 0.0001 | 0.05 | 0.04 | | | |
| Beat-and-glide | 0.0001 | | 0.04 | | | |
| **CEN** | | | | | | |
| Double-coiling | 0.0001 | 0.0005 | | 0.05 | - | - |
| Beat-and-glide | 0.005 | | | 0.05 | | |
| **IED** | | | | | | |
| Double-coiling | 0.005 | 0.15 | | | 0.005 | - |
| Beat-and-glide | 0.005 | | | | 0.005 | |
| **IIA** | 0 | 0 | 0 | 0 | 0 | 0 |

**Table 3.** *Chemical synapse (glutamatergic in white and glycinergic in gray) weights between neuron populations. Pre-synaptic neurons are in rows. Post-synaptic neurons in columns.*

| Pre-synaptic | Post-synaptic | | | | | | |
|---|---|---|---|---|---|---|---|
| | **MN** | **PM** | **CIN** | **CEN** | **IED** | **IIA** | **Muscle** |
| **MN** | | | | | | | |
| Single coiling | | | | | | | 0.015 |
| Double coiling | | | | | | | 0.02 |
| Beat-and-glide (base) | | | | | | | 0.1 |
| Beat-and-glide (bursting IED) | | | | | | | 0.1 |
| **CIN** | | | | | | | |
| Single coiling | 0.3 | 0.3 | | | | | |
| Double coiling | 2.0 | 2.0 | | | 2.0 | | |
| Beat-and-glide (base) | 1.5 | | 0.25 | | 1.5 | | |
| Beat-and-glide (bursting IED) | 1.5 | | 0.25 | | 3.0 | | |
| **CEN** | | | | | | | |
| Double coiling | | 0.175 | | | | | |
| Beat-and-glide (base) | | | | | 0.4 | | |
| Beat-and-glide (bursting IED) | | | | | 0.75 | | |
| **IED** | | | | | | | |
| Double coiling | | | | 0.04 | | | |
| Beat-and-glide (base) | 0.5 | | 0.3 | 0.25 | 0.3 | 0.5 | |
| Beat-and-glide (bursting IED) | 0.3 | | 0.225 | 0.15 | 0.3 | 0.2 | |
| **IIA** | | | | | | | |
| Beat-and-glide (base) | 1.0 | | 0.2 | 0.1 | 0.75 | | |
| Beat-and-glide (bursting IED) | 0.5 | | 0.2 | 0.1 | 0.5 | | |

**Table 4.** *Glutamatergic and glycinergic reversal potentials and time constants*

| Chemical Synapse | $E_{rev}$ | $\tau_r$ | $\tau_f$ | $V_{thr}$ |
|---|---|---|---|---|
| **Glutamatergic** | 0 | 0.5 | 1.0 | -15 |
| **Glycinergic** | -45, -58, -70* | 0.5 | 1.0 | -15 |

* *for single and double coiling and beat-and-glide swimming models, respectively*

*Supp. Data video S1* Single coiling model
*Supp. Data video S2* Truncated coils
*Supp. Data video S3* Double coiling model
*Supp. Data video S4* Glutamate null double coiling model
*Supp. Data video S5* Overexcited CEN double coiling model
*Supp. Data video S6* Glycine null double coiling model
*Supp. Data video S7* Beat-and-glide model
*Supp. Data video S8* IED knockout beat-and-glide model
*Supp. Data video S9* CEN knockout beat-and-glide model
*Supp. Data video S10* IIA knockout beat-and-glide model
*Supp. Data video S11 CIN* knockout beat-and-glide model
*Supp. Data video S12* Beat-and-glide with bursting IED model
*Supp. Data video S13* Swimming model with only tonic neurons
*Supp. Data video S14* Glycine null beat-and-glide model

## REFERENCES


Ampatzis, K., Song, J., Ausborn, J., & El Manira, A. (2013). Pattern of Innervation and Recruitment of Different Classes of Motoneurons in Adult Zebrafish. *Journal of Neuroscience*, *33*(26), 10875–10886. https://doi.org/10.1523/JNEUROSCI.0896-13.2013

Ampatzis, K., Song, J., Ausborn, J., & ElManira, A. (2014). Separate Microcircuit Modules of Distinct V2a Interneurons and Motoneurons Control the Speed of Locomotion. *Neuron*, *83*(4), 934–943. https://doi.org/10.1016/j.neuron.2014.07.018

Anderson, T. M., Abbinanti, M. D., Peck, J. H., Gilmour, M., Brownstone, R. M., & Masino, M. A. (2012). Low-threshold calcium currents contribute to locomotor-like activity in neonatal mice. *Journal of Neurophysiology*, *107*(1), 103–113. https://doi.org/10.1152/jn.00583.2011

Ausborn, J., Shevtsova, N. A., Caggiano, V., Danner, S. M., & Rybak, I. A. (2019). Computational modeling of brainstem circuits controlling locomotor frequency and gait. *ELife*, *8*. https://doi.org/10.7554/eLife.43587

Bagnall, M. W., & McLean, D. L. (2014). Modular organization of axial microcircuits in zebrafish. *Science*, *343*(6167), 197–200. https://doi.org/10.1126/science.1245629

Ben-Ari, Y. (2002). Excitatory actions of GABA during development: The nature of the nurture. *Nature Reviews Neuroscience*, *3*(9), 728–739. https://doi.org/10.1038/nrn920

Bennett, M. V. L., & Zukin, R. S. (2004). Electrical Coupling and Neuronal Synchronization in the Mammalian Brain. *Neuron*. https://doi.org/10.1016/S0896-6273(04)00043-1

Bernhardt, R. R., Chitnis, A. B., Lindamer, L., & Kuwada, J. Y. (1990). Identification of spinal neurons in the embryonic and larval zebrafish. *Journal of Comparative Neurology*. https://doi.org/10.1002/cne.903020315

Bicanski, A., Ryczko, D., Cabelguen, J.-M., & Ijspeert, A. J. (2013). From lamprey to salamander: An exploratory modeling study on the architecture of the spinal locomotor networks in the salamander. *Biological Cybernetics*, *107*(5), 565–587. https://doi.org/10.1007/s00422-012-0538-y

Björnfors, E. R., & El Manira, A. (2016). Functional diversity of excitatory commissural interneurons in adult zebrafish. *ELife*. https://doi.org/10.7554/eLife.18579

Buss, R. R., & Drapeau, P. (2000). Physiological properties of zebrafish embryonic red and white muscle fibers during early development. *Journal of Neurophysiology*.

Callahan, R. A., Roberts, R., Sengupta, M., Kimura, Y., Higashijima, S.-I., & Bagnall, M. W. (2019). Spinal V2b neurons reveal a role for ipsilateral inhibition in speed control. *ELife*, *8*. https://doi.org/10.7554/eLife.47837

Danner, S. M., Zhang, H., Shevtsova, N. A., Borowska-Fielding, J., Deska-Gauthier, D., Rybak, I. A., & Zhang, Y. (2019). Spinal V3 Interneurons and Left-Right Coordination in Mammalian Locomotion. *Frontiers in Cellular Neuroscience*, *13*, 516. https://doi.org/10.3389/fncel.2019.00516

Domenici, P., & Hale, M. E. (2019). Escape responses of fish: A review of the diversity in motor control, kinematics and behaviour. *Journal of Experimental Biology*, *222*(18). https://doi.org/10.1242/jeb.166009

Drapeau, P., Saint-Amant, L., Buss, R. R., Chong, M., McDearmid, J. R., & Brustein, E. (2002). Development of the locomotor network in zebrafish. *Progress in Neurobiology*, *68*(2), 85–111. https://doi.org/10.1016/S0301-0082(02)00075-8

Eklof-Ljunggren, E., Haupt, S., Ausborn, J., Dehnisch, I., Uhlen, P., Higashijima, S. -i., & El Manira, A. (2012). Origin of excitation underlying locomotion in the spinal circuit of

zebrafish. *Proceedings of the National Academy of Sciences*, *109*(14), 5511–5516. https://doi.org/10.1073/pnas.1115377109

Favero, M., Cangiano, A., & Busetto, G. (2014). The timing of activity is a regulatory signal during development of neural connections. *Journal of Molecular Neuroscience*, *53*(3), 324–329. https://doi.org/10.1007/s12031-013-0128-z

Goldman, M. S., Golowasch, J., Marder, E., & Abbott, L. F. (2001). Global Structure, Robustness, and Modulation of Neuronal Models. *The Journal of Neuroscience*, *21*(14), 5229–5238. https://doi.org/10.1523/JNEUROSCI.21-14-05229.2001

Golowasch, J., & Marder, E. (1992). Ionic currents of the lateral pyloric neuron of the stomatogastric ganglion of the crab. *Journal of Neurophysiology*, *67*(2), 318–331. https://doi.org/10.1152/jn.1992.67.2.318

Higashijima, S. I., Mandel, G., & Fetcho, J. R. (2004). Distribution of prospective glutamatergic, glycinergic, and gabaergic neurons in embryonic and larval zebrafish. *Journal of Comparative Neurology*, *480*(1), 1–8. https://doi.org/10.1002/cne.20278

Hull, M. J., Soffe, S. R., Willshaw, D. J., & Roberts, A. (2016). Modelling Feedback Excitation, Pacemaker Properties and Sensory Switching of Electrically Coupled Brainstem Neurons Controlling Rhythmic Activity. *PLoS Computational Biology*, *12*(1), e1004702. https://doi.org/10.1371/journal.pcbi.1004702

Izhikevich, E. M. (2007). *Dynamical Systems in Neuroscience: The Geometry of Excitability and Bursting*. The MIT Press.

Kimmel, C. B., Warga, R. M., & Kane, D. A. (1994). Cell cycles and clonal strings during formation of the zebrafish central nervous system. *Development (Cambridge, England)*, *120*(2), 265–276.

Kimmel, C. B., Ballard, W. W., Kimmel, S. R., Ullmann, B., & Schilling, T. F. (1995). Stages of embryonic development of the zebrafish. *Developmental Dynamics*, *203*(3), 253–310. https://doi.org/10.1002/aja.1002030302

Kimura, Y., & Higashijima, S.-I. (2019). Regulation of locomotor speed and selection of active sets of neurons by V1 neurons. *Nature Communications*, *10*(1), 2268. https://doi.org/10.1038/s41467-019-09871-x

Knogler, L. D., Ryan, J., Saint-Amant, L., & Drapeau, P. (2014). A Hybrid Electrical/Chemical Circuit in the Spinal Cord Generates a Transient Embryonic Motor Behavior. *Journal of Neuroscience*, *34*(29), 9644–9655. https://doi.org/10.1523/JNEUROSCI.1225-14.2014

Kozlov, A. K., Kardamakis, A. A., Hellgren Kotaleski, J., & Grillner, S. (2014). Gating of steering signals through phasic modulation of reticulospinal neurons during locomotion. *Proceedings of the National Academy of Sciences*, *111*(9), 3591–3596. https://doi.org/10.1073/pnas.1401459111

Lambert, A. M., Bonkowsky, J. L., & Masino, M. A. (2012). The Conserved Dopaminergic Diencephalospinal Tract Mediates Vertebrate Locomotor Development in Zebrafish Larvae. *Journal of Neuroscience*, *32*(39), 13488–13500. https://doi.org/10.1523/JNEUROSCI.1638-12.2012

Liao, J. C., & Fetcho, J. R. (2008). Shared versus Specialized Glycinergic Spinal Interneurons in Axial Motor Circuits of Larval Zebrafish. *Journal of Neuroscience*, *28*(48), 12982–12992. https://doi.org/10.1523/JNEUROSCI.3330-08.2008

Liu, D. W., & Westerfield, M. (1988). Function of identified motoneurones and coordination of primary and secondary motor systems during zebra fish swimming. *The Journal of Physiology*, *403*(1), 73–89. https://doi.org/10.1113/jphysiol.1988.sp017239

Ljunggren, E. E., Haupt, S., Ausborn, J., Ampatzis, K., & El Manira, A. (2014). Optogenetic Activation of Excitatory Premotor Interneurons Is Sufficient to Generate Coordinated Locomotor Activity in Larval Zebrafish. *Journal of Neuroscience*, *34*(1), 134–139. https://doi.org/10.1523/JNEUROSCI.4087-13.2014

McDearmid, J. J. R., & Drapeau, P. (2006). Rhythmic Motor Activity Evoked by NMDA in the Spinal Zebrafish Larva. *Journal of Neurophysiology*, *95*(1), 401–417. https://doi.org/10.1152/jn.00844.2005

McLean, D. L., & Fetcho, J. R. (2009). Spinal Interneurons Differentiate Sequentially from Those Driving the Fastest Swimming Movements in Larval Zebrafish to Those Driving the Slowest Ones. *Journal of Neuroscience*. https://doi.org/10.1523/jneurosci.3277-09.2009

McLean, D. L., Fan, J., Higashijima, S. I., Hale, M. E., & Fetcho, J. R. (2007). A topographic map of recruitment in spinal cord. *Nature*, *446*(7131), 71–75. https://doi.org/10.1038/nature05588

McLean, D. L., Masino, M. A., Koh, I. Y. Y., Lindquist, W. B., & Fetcho, J. R. (2008). Continuous shifts in the active set of spinal interneurons during changes in locomotor speed. *Nature Neuroscience*, *11*(12), 1419–1429. https://doi.org/10.1038/nn.2225

Menelaou, E., & McLean, D. L. (2012). A Gradient in Endogenous Rhythmicity and Oscillatory Drive Matches Recruitment Order in an Axial Motor Pool. *Journal of Neuroscience*, *32*(32), 10925–10939. https://doi.org/10.1523/JNEUROSCI.1809-12.2012

Menelaou, E., & McLean, D. L. (2019). Hierarchical control of locomotion by distinct types of spinal V2a interneurons in zebrafish. *Nature Communications*, *10*(1), 4197. https://doi.org/10.1038/s41467-019-12240-3

Myers, P. Z., Eisen, J. S., & Westerfield, M. (1986). Development and axonal outgrowth of identified motoneurons in the zebrafish. *The Journal of Neuroscience : The Official Journal of the Society for Neuroscience*, *6*(8), 2278–2289. https://doi.org/10.1523/JNEUROSCI.06-08-02278.1986

Roussel, Y., Paradis, M., Gaudreau, S. F., Lindsey, B. W., & Bui, T. V. (2020). Spatiotemporal Transition in the Role of Synaptic Inhibition to the Tail Beat Rhythm of Developing Larval Zebrafish. *ENeuro*, *7*(1). https://doi.org/10.1523/ENEURO.0508-18.2020

Saint-Amant, L. (2010). *Development of motor rhythms in zebrafish embryos* (Vol. 187). Elsevier B.V. https://doi.org/10.1016/B978-0-444-53613-6.00004-6

Saint-Amant, L., & Drapeau, P. (1998). Time course of the development of motor behaviors in the zebrafish embryo. *Journal of Neurobiology*, *37*(4), 622–632. https://doi.org/10.1002/(SICI)1097-4695(199812)37:4<622::AID-NEU10>3.0.CO;2-S

Saint-Amant, L., & Drapeau, P. (2000). Motoneuron activity patterns related to the earliest behavior of the zebrafish embryo. *The Journal of Neuroscience : The Official Journal of the Society for Neuroscience*, *20*(11), 3964–3972.

Saint-Amant, L., & Drapeau, P. (2001). Synchronization of an embryonic network of identified spinal interneurons solely by electrical coupling. *Neuron*, *31*(6), 1035–1046. https://doi.org/10.1016/S0896-6273(01)00416-0

Satou, C., Kimura, Y., & Higashijima, S. (2012). Generation of multiple classes of V0 neurons in zebrafish spinal cord: Progenitor heterogeneity and temporal control of neuronal diversity. *The Journal of Neuroscience: The Official Journal of the Society for Neuroscience*, *32*(5), 1771–1783. https://doi.org/10.1523/JNEUROSCI.5500-11.2012

Satou, C., Sugioka, T., Uemura, Y., Shimazaki, T., Zmarz, P., Kimura, Y., & Higashijima, S.-I.

(2020). Functional Diversity of Glycinergic Commissural Inhibitory Neurons in Larval Zebrafish. *Cell Reports*, *30*(9), 3036-3050.e4. https://doi.org/10.1016/j.celrep.2020.02.015

Sautois, B., Soffe, S. R., Li, W.-C., & Roberts, A. (2007). Role of type-specific neuron properties in a spinal cord motor network. *Journal of Computational Neuroscience*, *23*(1), 59–77. https://doi.org/10.1007/s10827-006-0019-1

Sengupta, M., Daliparthi, V., Roussel, Y., Bui, T. V., & Bagnall, M. W. (2021). Spinal V1 neurons inhibit motor targets locally and sensory targets distally to coordinate locomotion. *BioRxiv*, 2021.01.22.427836. https://doi.org/10.1101/2021.01.22.427836

Song, J., Dahlberg, E., & El Manira, A. (2018). V2a interneuron diversity tailors spinal circuit organization to control the vigor of locomotor movements. *Nature Communications*, *9*(1), 1–14. https://doi.org/10.1038/s41467-018-05827-9

Song, J., Pallucchi, I., Ausborn, J., Ampatzis, K., Bertuzzi, M., Fontanel, P., Picton, L. D., & El Manira, A. (2020). Multiple Rhythm-Generating Circuits Act in Tandem with Pacemaker Properties to Control the Start and Speed of Locomotion. *Neuron*. https://doi.org/10.1016/j.neuron.2019.12.030

Tazerart, S., Viemari, J.-C., Darbon, P., Vinay, L., & Brocard, F. (2007). Contribution of Persistent Sodium Current to Locomotor Pattern Generation in Neonatal Rats. *Journal of Neurophysiology*, *98*(2), 613–628. https://doi.org/10.1152/jn.00316.2007

Tong, H., & McDearmid, J. R. (2012). Pacemaker and plateau potentials shape output of a developing locomotor network. *Current Biology*, *22*(24), 2285–2293. https://doi.org/10.1016/j.cub.2012.10.025

Wahlstrom-Helgren, S., Montgomery, J. E., Vanpelt, K. T., Biltz, S. L., Peck, J. H., & Masino,

M. A. (2019). Glutamate receptor subtypes differentially contribute to optogenetically activated swimming in spinally transected zebrafish larvae. *Journal of Neurophysiology*, *122*(6), 2414–2426. https://doi.org/10.1152/jn.00337.2019

Warp, E., Agarwal, G., Wyart, C., Friedmann, D., Oldfield, C. S., Conner, A., Del Bene, F., Arrenberg, A. B., Baier, H., & Isacoff, E. Y. (2012). Emergence of patterned activity in the developing zebrafish spinal cord. *Current Biology: CB*, *22*(2), 93–102. https://doi.org/10.1016/j.cub.2011.12.002

Wiggin, T. D., Anderson, T. M., Eian, J., Peck, J. H., & Masino, M. A. (2012). Episodic swimming in the larval zebrafish is generated by a spatially distributed spinal network with modular functional organization. *Journal of Neurophysiology*, *108*(3), 925–934. https://doi.org/10.1152/jn.00233.2012

Wiggin, Timothy D., Peck, J. H., & Masino, M. A. (2014). Coordination of fictive motor activity in the larval zebrafish is generated by non-segmental mechanisms. *PLoS ONE*, *9*(10). https://doi.org/10.1371/journal.pone.0109117

Zhong, G., Masino, M. A., & Harris-Warrick, R. M. (2007). Persistent Sodium Currents Participate in Fictive Locomotion Generation in Neonatal Mouse Spinal Cord. *Journal of Neuroscience*, *27*(17), 4507–4518. https://doi.org/10.1523/JNEUROSCI.0124-07.2007